)

PARAMETERIZATION OF CONVECTION IN A ROTATING STRATIFIED OCEAN: COMPARISON OF NUMERICAL AND LABORATORY EXPERIMENTS WITH THEORY

by

Gwyneth Ellin Hufford

B.S.(Hons.) Pennsylvania State University
(1990)

Submitted in partial fulfillment of the
requirements for the degree of

Master of Science

at the

MASSACHUSETTS INSTITUTE OF TECHNOLOGY

and the

WOODS HOLE OCEANOGRAPHIC INSTITUTION

February 1995

© Gwyneth E. Hufford, 1994

Signature of Author . . . . . .
Joint Program in Physical Oceanography
Massachusetts Institute of Technology
Woods Hole Oceanographic Institution
September 30, 1994

Certified by . . . .
John C. Marshall
Professor of Physical Oceanography
Thesis Supervisor

Accepted by . . . .
Carl Wunsch
Chairman, Joint Committee for Physical Oceanography
Massachusetts Institute of Technology
Woods Hole Oceanographic Institution

Report Documentation Page		

1. REPORT DATE **FEB 1995**	2. REPORT TYPE	3. DATES COVERED **00-00-1995 to 00-00-1995**
4. TITLE AND SUBTITLE **Parameterization of Convection in a Rotating Stratified Ocean: Comparison of Numerical and Laboratory Experiments with Theory**		5a. CONTRACT NUMBER
		5b. GRANT NUMBER
		5c. PROGRAM ELEMENT NUMBER
6. AUTHOR(S)		5d. PROJECT NUMBER
		5e. TASK NUMBER
		5f. WORK UNIT NUMBER
7. PERFORMING ORGANIZATION NAME(S) AND ADDRESS(ES) **Massachusetts Institute of Technology,77 Massachusetts Avenue,Cambridge,MA,02139**		8. PERFORMING ORGANIZATION REPORT NUMBER
9. SPONSORING/MONITORING AGENCY NAME(S) AND ADDRESS(ES)		10. SPONSOR/MONITOR'S ACRONYM(S)
		11. SPONSOR/MONITOR'S REPORT NUMBER(S)

12. DISTRIBUTION/AVAILABILITY STATEMENT **Approved for public release; distribution unlimited**

13. SUPPLEMENTARY NOTES

14. ABSTRACT

Laboratory and numerical experiments are carried out in a parameter regime relevant to open-ocean deep convection. We consider the case of convection in a rotating stratified ocean of finite depth. Convection is induced from the surface by extracting buoyancy over a circular area. The external parameters are buoyancy forcing of strength B,, applied over a circular area of radius R,, the rotation rate is measured by f, ambient stratification N and finite depth H. Theoretical scaling predictions are derived to describe the length and velocity scales of the convective chimney as it adjusts under gravity and rotation, and breaks up through baroclinic instability. The scales of interest include the number (M), size (leddy) and strength (Urim) of the baroclinic eddies formed. Also of interest are the final depth of penetration of the convective mixed layer (dfinal) and the final volume of convectively produced water (Vinal). These scales are tested against the laboratory and numerical experiments and found to be appropriate. We show that for this idealized problem dfinal depends only on the size and strength of the forcing and the ambient stratification encountered by the convection event; it does not depend explicitly on rotation. The volume of convectively modified water produced continues to increase as long as forcing continues, but the rate of production depends again only on the size and strength of the forcing and on the ambient stratification. The implications of the work to deep water formation in the Labrador Sea and elsewhere are discussed. Finally the study has relevance to the role and representation of baroclinic eddies in large-scale circulation of the ocean.

15. SUBJECT TERMS					
16. SECURITY CLASSIFICATION OF:			17. LIMITATION OF ABSTRACT	18. NUMBER OF PAGES	19a. NAME OF RESPONSIBLE PERSON
a. REPORT **unclassified**	b. ABSTRACT **unclassified**	c. THIS PAGE **unclassified**	**Same as Report (SAR)**	**75**	

PARAMETERIZATION OF CONVECTION IN A ROTATING STRATIFIED OCEAN: COMPARISON OF NUMERICAL AND LABORATORY EXPERIMENTS WITH THEORY

by

Gwyneth Ellin Hufford

Submitted in partial fulfillment of the requirements for the degree of
Master of Science at the Massachusetts Institute of Technology
and the Woods Hole Oceanographic Institution
September 30, 1994

Abstract

Laboratory and numerical experiments are carried out in a parameter regime relevant to open–ocean deep convection. We consider the case of convection in a rotating stratified ocean of finite depth. Convection is induced from the surface by extracting buoyancy over a circular area. The external parameters are buoyancy forcing of strength B_o applied over a circular area of radius R_s, the rotation rate is measured by f, ambient stratification N and finite depth H. Theoretical scaling predictions are derived to describe the length and velocity scales of the convective chimney as it adjusts under gravity and rotation, and breaks up through baroclinic instability. The scales of interest include the number (M), size (l_{eddy}) and strength (u_{rim}) of the baroclinic eddies formed. Also of interest are the final depth of penetration of the convective mixed layer (d_{final}) and the final volume of convectively produced water (V_{final}). These scales are tested against the laboratory and numerical experiments and found to be appropriate. We show that for this idealized problem d_{final} depends only on the size and strength of the forcing and the ambient stratification encountered by the convection event; it does not depend explicitly on rotation. The volume of convectively modified water produced continues to increase as long as forcing continues, but the rate of production depends again only on the size and strength of the forcing and on the ambient stratification. The implications of the work to deep water formation in the Labrador Sea and elsewhere are discussed. Finally, the study has relevance to the role and representation of baroclinic eddies in large–scale circulation of the ocean.

Acknowledgements

Contents

Chapter 1

Introduction

1.1 Dynamics of chimney convection

This study is an attempt to better understand the process of open ocean deep convection. It is a complex phenomenon comprised of many aspects only some of which are well understood. In this study we set up and study a highly idealized, but physically relevant system: convection in a stratified rotating fluid, driven by buoyancy loss over a circular area at the surface. Length, time and velocity scales for the key processes are deduced, as well as what we believe are the relevant non-dimensional numbers describing the physics involved. Finally, we test the appropriateness of the scalings by laboratory and numerical experiment.

Open ocean deep convection is the phenomenon by which surface water is made dense through cooling and/or salinification and subsequently sinks, sometimes to great depth. The externally imposed parameters are the buoyancy forcing, the background stratification of the fluid, the rotation of the Earth, and the total depth of the ocean. Buoyancy forcing is characterized by a magnitude B_o (m^2/s^3), (related for example to heat flux by the relation $Q = \frac{B_o \rho c_p}{g \alpha}$), applied over a circular area of radius R_s (m). Stratification is measured by the Brunt-Vaisala frequency $N = \left(\frac{g \Delta \rho}{\rho_o \Delta z} \right)^{1/2}$ (s^{-1}), rotation by the Coriolis frequency f (s^{-1}). Finally, ocean depth is denoted
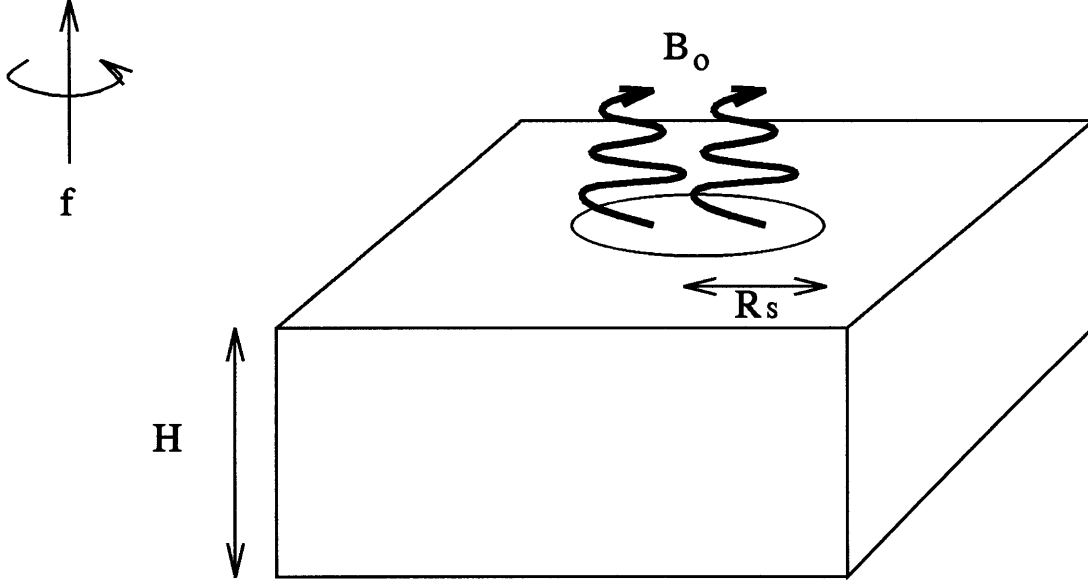
Figure 1.1: A schematic representation of the idealized convection model under consideration. Buoyancy (B_o) is extracted over a circular region at the surface with radius R_s. The total depth is fixed at H. There are no horizontal boundaries affecting horizontal evolution; all experiments are terminated before side wall effects interfere. The entire system is under rotation, f.

here by H (m). These parameters are all shown schematically in Figure 1.1. In addition to these parameters, it will be necessary to consider briefly the viscosity and diffusivity of the fluid, ν and κ (m^2/s).

From these parameters, considered together with time t (s), we can deduce other scales for the features of a convective event. The buoyancy forcing drives isolated overturning cells called plumes, some of the details of which are described in the review article [Marshall, Whitehead and Yates, 1994] and [Jones and Marshall, 1993]. These plumes, perhaps less than 1 km in diameter, act in concert to form a chimney of well mixed dense fluid as seen in Figures 1.2 through 1.5. This chimney may be many, perhaps hundreds of plumes wide. Figure 1.3 shows a chimney observed in the Mediterranean Sea. This event was observed by [THETIS, 1994] during February 1992. The contours shown here are potential density, sigma-theta. Figure 1.4 shows the phenomenon in the laboratory. Figure 1.5 shows a cross section from one
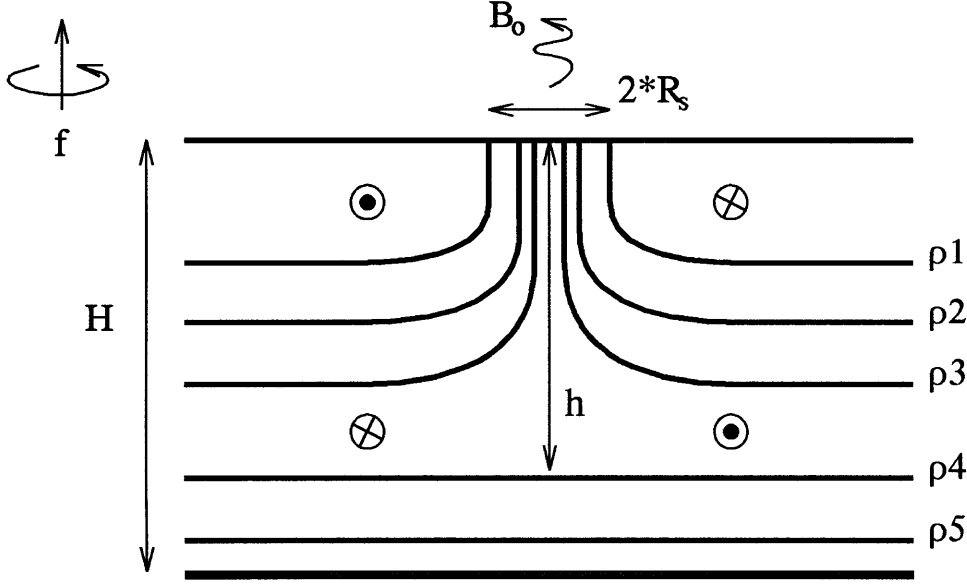
Figure 1.2: Schematic diagram of a typical convection event cross section. Note the depth scale measured from the surface to the spreading level.

of our numerical experiments. Figure 1.2 shows a schematic of the chimney cross section, illustrating our particular interest in those processes which control the depth, h, reached by the convectively produced mixed layer.

Strong horizontal density gradients are set up across the wall of the chimney where isopycnals bow up from depth to the sea surface. Under the influences of rotation the chimney begins to adjust to geostrophic balance. At the surface, convergence results in a cyclonic rim current; at depth, divergence results in an anti-cyclonic rim current. These circulations are also shown in Figure 1.2.

The opposing currents at the surface and at depth are associated, by thermal wind, with horizontal buoyancy gradients. The resulting vertical shear leads to baroclinic instability. If the horizontal extent of the chimney exceeds the Rossby radius of deformation the chimney will break up into smaller, Rossby-radius scale eddies. This breakup is illustrated in Figures 1.6 through 1.9 . Figure 1.6 shows a schematic of the horizontal evolution of the chimney, illustrating the horizontal scales we wish to investigate: u_{rim} (m/s) the velocity of the rim current, l_{eddy} (m) the length scale

7
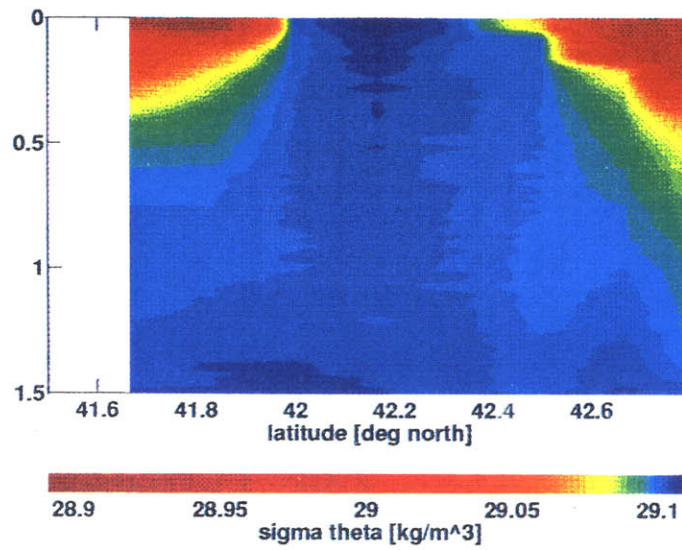
Figure 1.3: [THETIS, 1994], cross section of Meditteranean convection event, seen using accoustic profiling.
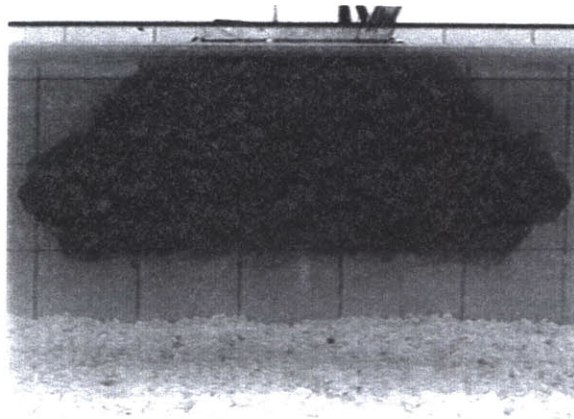
Figure 1.4: Photograph of laboratory experiment; shown here is a typical cross section. Note the constriction of the chimney near the source, and the spreading level at depth.
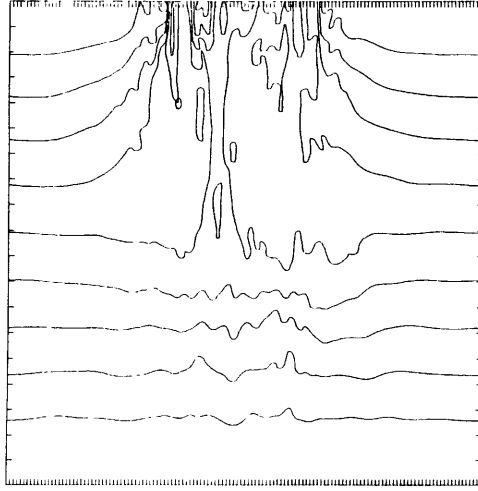
Figure 1.5: Cross section plotted from numerical model; shown here are the salt contours. Recall that temperature is held constant in the model, so that isohalines are equivalent to isopycnals.

the baroclinic eddies, and M, the number of eddies formed. Figure 1.7 shows a salinity map from a [MEDOC, 1970] surveyed convection site. Figure 1.8 shows an overhead view of convection in the laboratory after the onset of instability. This event is a typical example of one of our high mode laboratory experiments. Photographs of lower mode instabilities will be presented below. Figure 1.9 shows the same phenomenon manifest in the numerical model results.

One objective of this thesis is to determine how the aforementioned scales depend on the externally imposed parameters and the non-dimensional numbers which govern the system. These non-dimensional numbers are chosen to be $R_o^* = \frac{\sqrt{B_o/f^3}}{H}$, the natural Rossby number which measures the significance of the distance over which rotation becomes important, versus the total depth of the fluid - for a review see, [Marshall, Whitehead and Yates, 1994], or [Maxworthy and Narimousa, 1994], N/f, relating stratification and rotation, and R_s/H, an aspect ratio comparing the size of the forcing area to the total depth of the fluid.

9
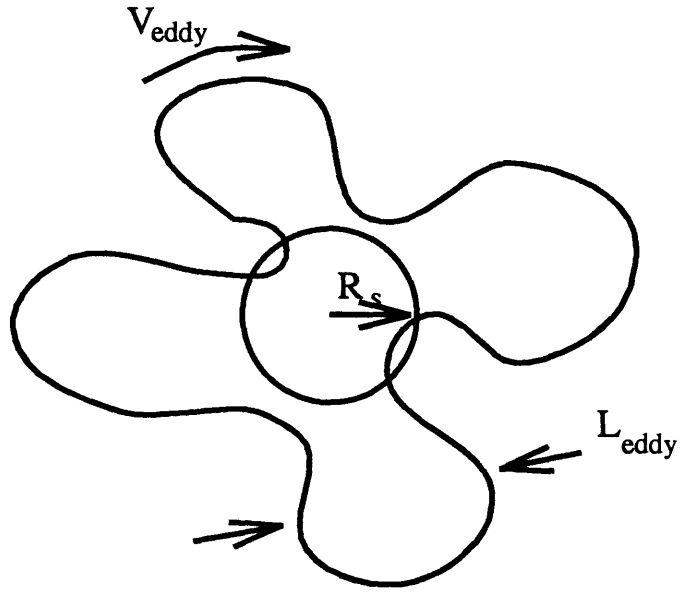
Figure 1.6: Schematic diagram of a typical convection event as seen from above, illustrating our interest in the number of eddies formed, their associated velocities and length scales.
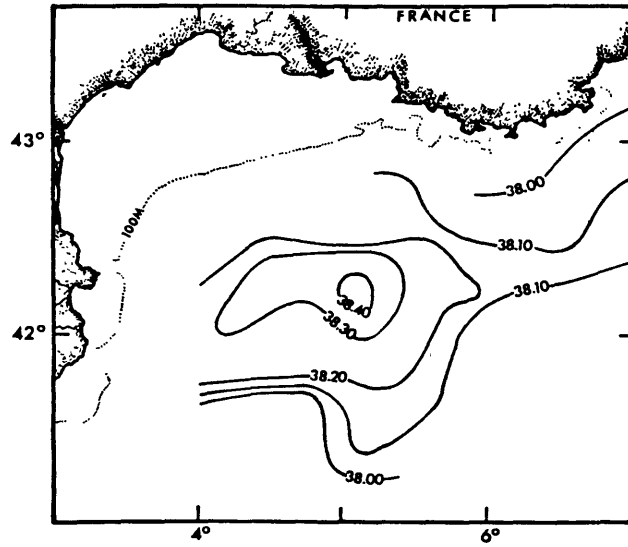
Figure 1.7: Salinity map showing a convection region in the Meditteranean Sea, surveyed hydrographically by [MEDOC, 1970]. Note the geometry and the horizontal scale of the convective patch - approximately 100 km.

10
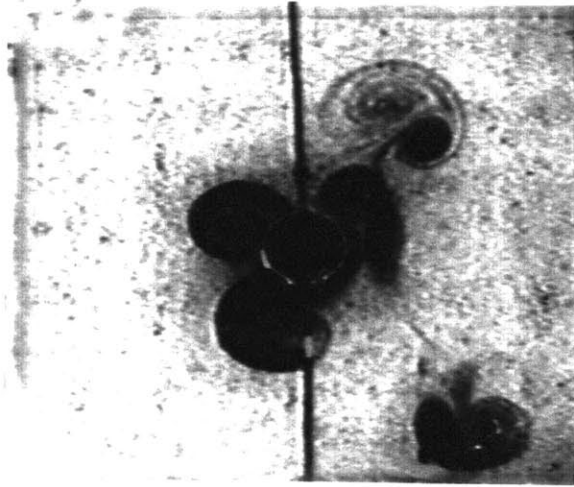
Figure 1.8: Photograph of laboratory experiment; shown here is a typical high mode laboratory experiment. Note particularly the distinct eddies migrating away from the source.
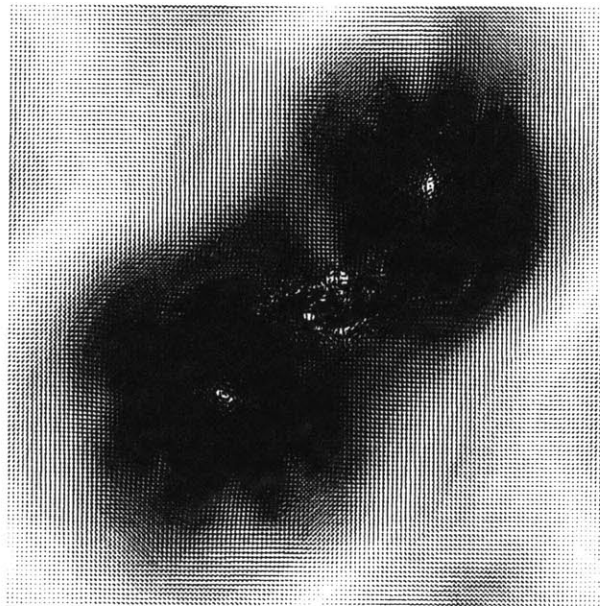
Figure 1.9: Horizontal map of numerical model velocity fields. Note the developed eddy circulations, allowing estimates of mode number, size and associated velocity.

To test the proposed scalings of h, u_{rim}, l_{eddy} and M, and determine the dependence of these scales on the non-dimensional numbers, we carried out laboratory and numerical experiments simulating our idealized physical system. The laboratory experiment consists of a rotating tank filled with linearly stratified fluid from which buoyancy is extracted over a circular area at the surface. The computational analog is a numerical simulation of the laboratory experiment using a non-hydrostatic primitive equation model [Brugge et al., 1991]. The study also provides an interesting context in which to compare in detail laboratory and numerical results.

In Chapter 2 we introduce non-dimensional numbers and the proposed scalings for h, u_{rim}, l_{eddy} and M. Chapter 3 presents the laboratory experiment, including method and results. Chapter 4 presents the numerical simulations of the laboratory experiments, including method, comparison with the laboratory, and further results. Chapter 5 is a discussion of our results in the context of the ocean.

Chapter 2

Scaling

2.1 Non-dimensional numbers

When an unstratified fluid of total depth H is forced to convect by uniform surface cooling in the presence of rotation (f), there is only one nondimensional combination of the main external parameters B_o, f and H: the natural Rossby number R_o^*.

$$R_o^* \sim \frac{\sqrt{B_o/f^3}}{H} \sim \frac{l_{rot}}{H}.$$

Here $l_{rot} = \sqrt{B_o/f^3}$ is the vertical scale to which convection penetrates in an unstratified fluid during an inertial period - the period when rotation becomes important. If R_o^* is large then the convection will be limited by the ocean depth before it feels the effects of rotation; if R_o^* is small then the convection will come under geostrophic control before encountering the bottom. Oceanic values of R_o^* in convective regions are typically small, placing the phenomenon in a regime where rotation may be important. In the ocean, typical values for f, B_o and H are: in the Mediterranean $f \approx 10^{-4}s^{-1}$, $B_o \approx 10^{-7}m^2/s^3$ (corresponding to a heat loss of ≈ 2000 W/m^2, where $B_o = \frac{g\alpha Q}{\rho c_p}$, α is is the thermal expansion coefficient for water, ρ is the density of water, c_p is the specific heat, g is the gravitational constant and Q is the heat loss, and $H \approx 2000m$ [Leaman and Schott] giving an R_o^* of 0.1; in the polar

seas these values are $f \approx 1.5 \times 10^{-4}s^{-1}$, $B_o \approx 10^{-7}m^2/s^3$, and $H \approx 1000 - 4000m$ [Marshall, Whitehead and Yates, 1994] giving an R_o^* of 0.01. Typical ocean values then are in the range of $0.01 < R_o^* < 0.1$. In the laboratory experiments presented here R_o^* ranges from 0.04-0.41. In our numerical experiments R_o^* varies from 0.05-0.58. In both cases the experiments span the oceanic regime.

In addition to R_o^* two additional non-dimensional numbers are needed to fully describe the system when stratification and a finite forcing length scale are included,

$$N/f$$

and

$$R_s/H.$$

The first describes the relative significance of rotation and stratification. The second is an aspect ratio describing the size of the forcing area compared to the depth of the water column. Values of N for the upper ocean are typically 0.01 s^{-1} in the high gradient regions, while values for the deep ocean may be as small as 0.001 s^{-1}, [Gill, 1982]. Typical values of f are of order $10^{-4}s^{-1}$. Thus the range of N/f for the ocean, specifically for convection regions is from order 1-10, while values for the rest of the ocean may be as high as $N/f \approx 50$. Deep convection sites are very weakly stratified, [Leaman and Schott]. In the laboratory we achieve a range of $0.86 < N/f < 6.64$; in the numerical experiments we achieve a range of $0.82 < N/f < 7.5$. This places the experiments described here in the lower limit of thermocline ocean values, making the experiments particularly suited to deep ocean convection sites. Note also that N/f spans an order of magnitude in the experiments to allow investigation of dependence of convection on this parameter. Typical length scales for R_s are set by meteorological forcing and in the ocean can range from small disturbance scales (eg. squall line) .5 km, to atmospheric meso-scale disturbances 100 km. Ocean values of H are 1000-4000 m. This gives a range of $.1 < R_s/H < 100$. In both the laboratory and the numerical experiments R_s/H spanned .25-.75. This

places the experiments again at the lower limit of the real ocean values, but still well within the range that makes them relevant to the real ocean.

One other non-dimensional number must be mentioned, that is the Rayleigh number, $Ra_f = \frac{B_o H^4}{\kappa^2 \nu}$. It relates the relevant forcing and stabilizing mechanisms involved in convective overturning. Buoyancy forcing at the surface establishes a density gradient; diffusion erodes that gradient. It is a well established result from Rayleigh's calculations that for a given stratification, diffusion, viscosity and depth there exists a critical value of forcing necessary to achieve overturning. In other words, there is a critical value of Ra_f necessary to achieve instability. For the simple problem of temperature difference between two plates, that number is

$$Ra_f(cr) = \frac{27\pi^4}{4} = 656.$$

This result is highly dependent on the boundary conditions. The result will also be affected by the presence of rotation. Rotation stiffens the fluid and inhibits overturning, then the critical value of Ra_f will be increased.

The critical value has been related to the Taylor number [Chandrasekhar, 1953] and [Nakagawa and Frenzen, 1955] according to the relationship

$$Ra_f(cr) = kTa^{2/3},$$

where k is a constant dependent on the boundary conditions, and Ta is the Taylor number $Ta = \frac{f^2 H^4}{\nu^2}$.

[Bubnov and Senatorsky, 1988] determined k experimentally and found it to lie between 2.39 and 8.72; the particular value depended strongly on the boundary conditions used. For the laboratory and numerical experiments studied here, $Ta \approx 10^5$ giving a critical Rayleigh number of $Ra_f(cr) = 10^6$.

The important point to be made is that there is a critical value of Ra_f necessary for convective overturning and that number $Ra_f(cr)$ is never larger than 10^6 at the upper limit. In our numerical and laboratory experiments we exceed that number by

several orders of magnitude. In the ocean, $f \approx 10^{-4}/s$, $H \approx 10^3 m$, $\nu \approx 10^{-6} m^2/s$ and $\kappa \approx 10^{-7} m^2/s$ (for thermal diffusion in water). This gives typical ocean values of $Ra_f \approx 10^{27}$ and $Ta \approx 10^{22}$.

In the laboratory it is impossible to achieve a value of H similar to that of the ocean. Ocean values of H may be obtained in the numerical experiments, but only at the price of increasing values of ν and κ. The increase in H is accompanied by a loss of resolution which must be compensated by increases in ν and κ to parameterize all unresolved mixing. So, using molecular values of ν and κ, typical laboratory values of Ra_f range from 10^{13} to 10^{15} where values of f range from .01 to .1/s and $H \approx .1m$ resulting in Ra_f.

In the numerical experiments a larger values of κ is used for numerical stability, $\kappa \approx 10^{-6} m^2/s$. So, the numerical system has a Prandtl number of one. Rotation can be increased more in the numerical experiments than in the laboratory, so $f \approx .01 - 1/s$. Values of Ra_f for the numerical experiments range from $10^7 - 10^{11}$.

In summary, it is impossible to achieve oceanic values of Ra_f in either the laboratory or the numerical experiments. However, it is still possible to gain useful information from the experiments because in both the laboratory and on the computer, the critical value of Ra_f is exceeded by several orders of magnitude, placing all three cases in the realm of convective instability. So, we can use laboratory and numerical experiments to systematically investigate convective instability and gain meaningful results which may be applied to ocean dynamics.

2.2   Convection in a stratified rotating ocean

We have chosen to study the problem of convection in a stratified rotating ocean with a finite depth. We will consider buoyancy forcing applied over a finite circular area only. In our highly idealized problem the parameters to be considered are: B_o, t, N, f, H, and R_s. Here again B_o (m^2/s^3) is the magnitude of the buoyancy forcing, t (s)

is time, N (s^{-1}) is the Brunt-Vaisala frequency and f (s^{-1}) the Coriolis frequency, $H(m)$ is the total depth of the ocean, and R_s is the radius of the buoyancy forcing patch.

Previous work [Legg and Marshall, 1994] [Jones and Marshall, 1993] has focused on the evolution of individual plumes. In the present study we concern ourselves with the development of the entire chimney which is made up of, and indeed created by, many plumes. The plumes act in concert to densify the surface water layer. The entire area of the chimney is mixed, the dense layer evolving with time. One premise of this scaling is that the deepening of the convective mixed layer is independent of the inhomogeneity introduced by the existence of the individual plumes. The assumption that the chimney evolves independent of the resolution of the plumes is supported by both laboratory and computer data and is discussed in Chapter 5. The chimney, if it is sufficiently large, will ultimately break up under baroclinic instability. Recall that the properties of the convective chimney which we have chosen to look at are h, u_{rim}, l_{eddy} and M.

Let us now consider the vertical evolution of the mixed layer at a position in the center of the well mixed chimney. A water parcel in this position will be unaware of any spatial inhomogeneity in either cooling or overturning.

Before rotation becomes important the evolution of the mixed layer can be described by a one dimensional model, assuming there is no lateral mixing across the boundary of the chimney. From the definition of heat flux, one can write

$$\mathcal{H} = h\rho c_p \left(-\frac{\partial T}{\partial z}\right)\left(\frac{\partial h}{\partial t}\right)$$

where h is the depth over which the fluid is mixed, T is temperature, and t is time and the time derivative of temperature has been written thus: $\frac{\partial T}{\partial t} = \frac{\partial T}{\partial z}\frac{\partial z}{\partial t}$. The resulting expression for buoyancy is:

$$B_o = -g\alpha h \left(\frac{\partial T}{\partial z}\right)\left(\frac{\partial h}{\partial t}\right),$$
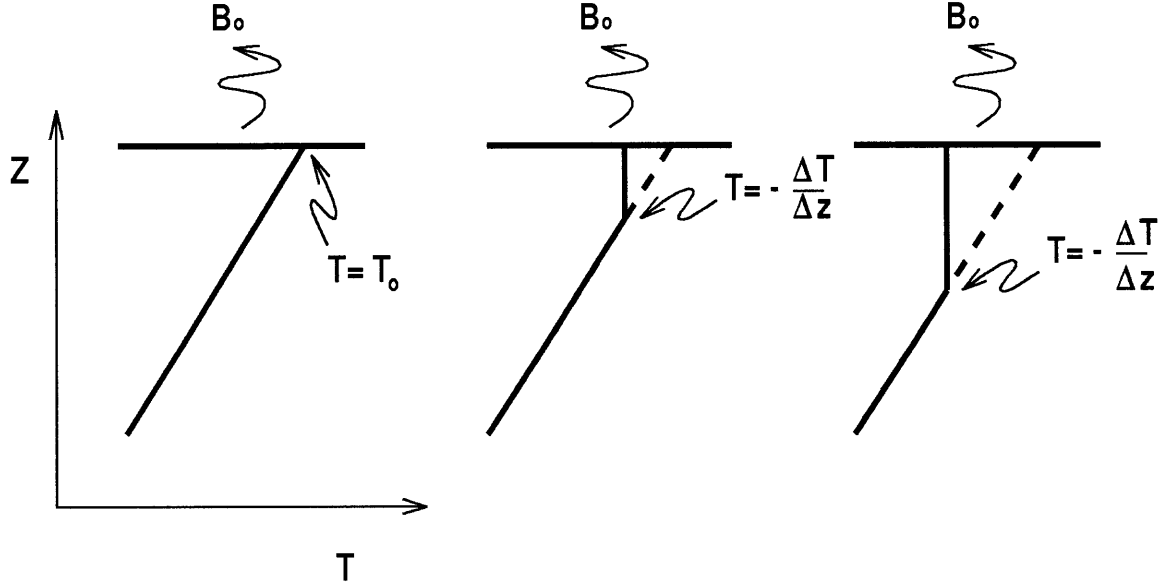
Figure 2.1: A schematic diagram of the one dimensional vertical evolution of a mixed layer driven by temperature forcing. Each graph represents a new time. As buoyancy is removed through the surface, the mixed layer extends to a larger depth.

where $B_o = \frac{g\alpha Q}{\rho c_p}$.

Grouping terms and using the definition of buoyancy frequency N,

$$N^2 = -g\alpha \frac{\partial T}{\partial z},$$

we find

$$B_o = N^2 h \frac{\partial h}{\partial t}.$$

Integrating and solving this equation for h gives the well-known result for the non-penetrative deepening of a mixed layer (see for example [Ivey et al., 1993]):

$$h = \sqrt{\frac{2B_o t}{N^2}}.$$

This derivation assumes only that the mixing is non-penetrative. The result suggests, as expected, that if N increases then h decreases; that is, larger stratification will impede the deepening of the mixed layer. It also suggests that for very small times h will increase rapidly, while for large times h increases much more slowly.

18

We might expect from geostrophic adjustment theory that the chimney wall has a width $R_D = \frac{Nh}{f}$, the Rossby radius of deformation. As rotation becomes important the chimney adjusts toward geostrophic balance. The surface convergence described in Chapter 1 has an associated cyclonic velocity, u_{rim}. Using thermal wind balance one can deduce u_{rim}:

$$\frac{du}{dz} = \frac{g}{\rho f}\left(\frac{\partial \rho}{\partial y}\right),$$

where u is the azimuthal velocity and $\frac{\partial \rho}{\partial y}$ indicates the density gradient across the chimney wall. Then

$$u_{rim} = \frac{gh}{\rho_o f}\frac{\Delta \rho_y}{\Delta y}.$$

We define the chimney geometry such that the density difference radially outward from the center is the same as the vertical density difference from the spreading level to the surface, see Figure 2.2. Then by definition $\Delta\rho_y = \Delta\rho_z$. So

$$\frac{g\rho'}{\rho_o} = N^2 h.$$

Substituting into our expression for u_{rim}

$$u_{rim} = \frac{hg\Delta\rho_z hL}{f\rho_o \Delta y hL} = \frac{N^2 h^2}{fL}$$

which, recalling that $L = \frac{Nh}{f}$, gives

$$u_{rim} \sim Nh.$$

Thus the rim current will continue to grow as h evolves in time, until the onset of baroclinic instability. At that time the eddies formed will transport water away from the chimney, violating the 1-d assumption of no lateral mixing.

The breakup time scale may be derived from the Eady result for baroclinic instability growth rate. The growth rate of the fastest growing mode is described by the complex part of the wave frequency; the result [Eady, 1949] being

$$kc_i \sim \frac{f}{\sqrt{R_i}}$$
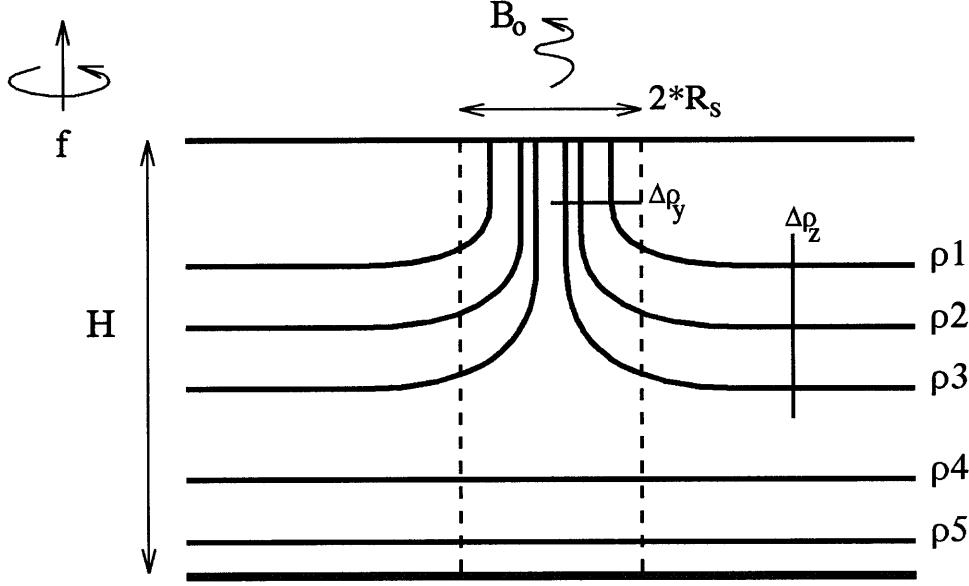
Figure 2.2: A schematic cross section through a chimney, illustrating the definitions of chimney geometry. Note especially the equivalence of the density differences from the center of the chimney to the outside, and from the spreading layer to the surface.

where $R_i = N^2 / \left(\frac{\partial u}{\partial z}\right)^2$.

Once again assuming thermal wind balance we can use the above result of $\frac{\partial u}{\partial z} \sim N$, ie. the $R_i = 1$, then

$$kc_i = f,$$

leading to a time scale $t \sim f^{-1}$.

At this time, $t \sim f^{-1}$ our derived scales become:

$$h \sim \sqrt{\frac{2B_o}{N^2 f}},$$

so

$$u_{rim} \sim Nh \sim \sqrt{2B_o/f},$$

and

$$L \sim \sqrt{2B_o/f^3}.$$

Interestingly, each of these quantities appears in terms of the fundamental scales governing the evolution of the individual plumes in an unstratified rotating

20

fluid [Jones and Marshall, 1993]:

$$l_{rot} \sim \sqrt{B_o/f^3}$$

$$u_{rot} \sim \sqrt{B_o/f}.$$

Then

$$h \sim \frac{u_{rot}}{N},$$

$$u_{rim} \sim u_{rot},$$

and

$$L \sim l_{rot}.$$

2.3   The equilibrium state

So the initial stages of the vertical evolution of the mixed layer are governed by the one dimensional result, which is valid until baroclinic instability sets in on a time-scale $t \sim f^{-1}$. At that time, the baroclinic instability drives exchange between the chimney and the surrounding region. This lateral exchange inhibits the further vertical evolution of the mixed layer, so that the depth with time curve now lies below the $t^{1/2}$ curve, see Figure 2.3. Eventually an equilibrium must be reached between the density forcing through the surface and the lateral removal of dense fluid by the baroclinic eddies, as detailed in [Legg and Marshall, 1994]. This equilibrium necessarily halts further deepening of the mixed layer; the depth at this time will be the maximum depth achieved and may derived as follows. The balance between the buoyancy flux through the surface and the lateral transport can be written as [Visbeck and Marshall, 1994]

$$\int \frac{B_o}{g} dA = \frac{1}{\rho} \int \oint \overline{u'\rho'} dl dZ,$$

where u is the horizontal cross stream velocity and the bar denotes a time average, indicating our desire to study the steady state. From energy analysis of the baroclinic

region we can write [Eady, 1949] [Green, 1970]

$$\overline{u'\rho'} = \frac{g}{N\rho_o}\rho'^2,$$

where ρ' is the perturbation density anomaly achieved when moving a water parcel in the baroclinic region. Since (as discussed above)

$$\frac{g\rho'}{\rho_o} = N^2 h,$$

$\overline{u'\rho'}$ may be written thus:

$$u'\rho' = \frac{\rho_o}{g}N^3 h.$$

Then our above integral balance becomes

$$\frac{1}{g}B_o \pi R_s^2 \sim \frac{1}{\rho_o}2\pi R_s N^3 h^3,$$

which reduces to

$$h \sim d_{final} \sim \frac{(B_o R_s)^{1/3}}{N}.$$

This is the quantity we call d_{final}, our scaling for the maximum depth achieved by the convective mixed layer, assuming all available potential energy is converted to kinetic energy. The resulting scaling for penetration depth says that d_{final} should depend only on the size of the source, the strength of the forcing and stratification. There is no f dependence. This prediction is strongly supported by the numerical data in Chapter 4.

Now let us go back and investigate the scales of the baroclinic instability, in the context of the evolution of the mixed layer. We know from the solution of Eady's baroclinic instability problem that

$$l_{eddy} \sim R_D \sim \frac{Nh}{f}.$$

As h increases then so must l_{eddy}, in accordance with the expressions derived above for h. The number of eddies present is dependent on the integral number of wavelengths that may be contained about the circumference of the chimney, that is

$$M = \frac{2\pi R_s^2}{l_{eddy}}.$$
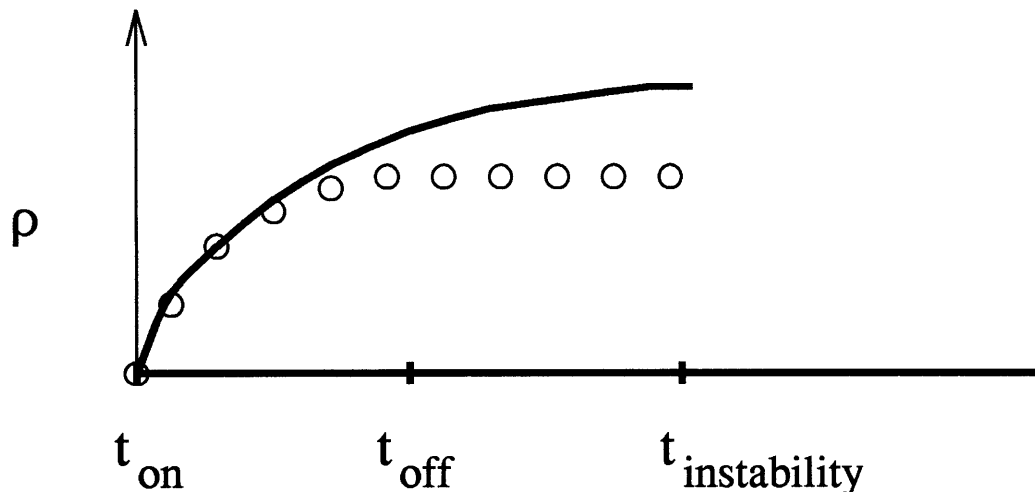
Figure 2.3: Plot illustrating the arrest of the vertical evolution of the mixed layer in the presence of baroclinic eddy transport. As the eddies move dense water away from the source area, the mixed layer ceases to deepen. This is manifest in a leveling off of the average salt content in a cylinder defined by the source area and the total depth of the water column.

Again, this number will change with time, as l_{eddy} grows. This prediction is borne out by the data as initially h is small and the chimney begins to break up into a large number of eddies. As time goes on, h increases and one sees the eddies coalesce. In the end, the number of eddies actually shed is smaller than the number of waves initially visible at the onset of instability. In fact, according to the analysis of the problem for a cylindrical geometry, carried out in [Legg and Marshall, 1994], the final result should be

$$M = \frac{\sqrt{8}R_s^2}{Nh/f}$$

where h is chosen appropriately.

To summarize we now have scalings for the velocity of the rim current in the baroclinic zone, the number of baroclinic eddies formed, their associated length scale and the final resting depth of the convectively produced dense water. These scaling predictions are hence forth denoted by the superscript 'scal':

$$u_{rim}^{scal} = Nh$$

23

$$l_{eddy}^{scal} = \frac{Nh}{f}$$

$$M^{scal} = \frac{\sqrt{8}R_s^2 f}{Nh}$$

and

$$d_{final}^{scal} = \frac{(R_s B_o)^{1/3}}{N}.$$

Finally, it is interesting to consider the final volume of dense water produced during a convection event. An upper limit on this number is given by the fastest rate at which dense water may be produced. The shortest time in which the system can reach d_{final} is given by the time it would take the one-dimensional model to evolve to d_{final}. Once the one-dimensional model ceases to be valid vertical evolution has slowed under the stiffness imposed by rotation. So, the shortest time necessary for the system to reach d_{final} is given by

$$h \sim d_{final}$$

$$\frac{\sqrt{2B_o t}}{N} \sim \frac{(B_o R_S)^{1/3}}{N}.$$

Solving this for t gives us:

$$\sqrt{t} \sim B_o^{-1/6} R_s^{1/3}$$

$$t \sim \left(\frac{R_s^2}{B_o}\right)^{1/3}.$$

Then the fastest rate at which dense water can be produced is the volume of the cylinder beneath the source, divided by this time:

$$rate_{max} = \frac{\pi R_s^2 d_{final}}{\left(\frac{R_s^2}{B_o}\right)^{1/3}},$$

$$rate_{max} \sim \pi R_s^{4/3} d_{final} B_o^{1/3}.$$

Then the largest amount of water produced by the event would be the fastest rate multiplied by the amount of time gone by; obviously the amount of water convectively produced will continue to increase as long as the forcing continues. So, we can imagine

that the cylinder will fill, no faster than the rate we calculated, then the dense water will be transported away and the process will begin again. We can expect the final volume of convectively produced water to follow the relation:

$$V_{final}^{scal} = rate_{max} * t.$$

This hypothesis is supported by the numerical data.

Chapter 3

The Laboratory Analog

3.1 Instrumental method

The laboratory apparatus was designed by Jack Whitehead, Bob Frazel and the author. The raw data were extracted from the tapes by Jack Whitehead. The statistical analysis was performed by the author. A square glass tank was used of dimension 114 cm x 114 cm x 60 cm, see Figure 3.1. The bottom of the tank is marine plywood. Dense fluid is introduced at the surface through a diffuser. Two types of diffuser are used depending on the source area required for a given run. Two video cameras are used to record the experiments, one at the side of the tank, the other rotating with the table, recording from above.

The tank is filled using a two reservoir method to achieve stratification. A fresh water reservoir is filled with one half the volume of the experimental tank. A second reservoir is also filled with one half the tank volume but has a density equal to the maximum density desired for the experimental tank. A valve connects the two reservoirs at their base. Water is drawn from the fresh reservoir and replaced from the salty reservoir. The result is linearly increasingly dense layers being set down in the tank, one beneath the other. The experimental tank is filled while it is turning,
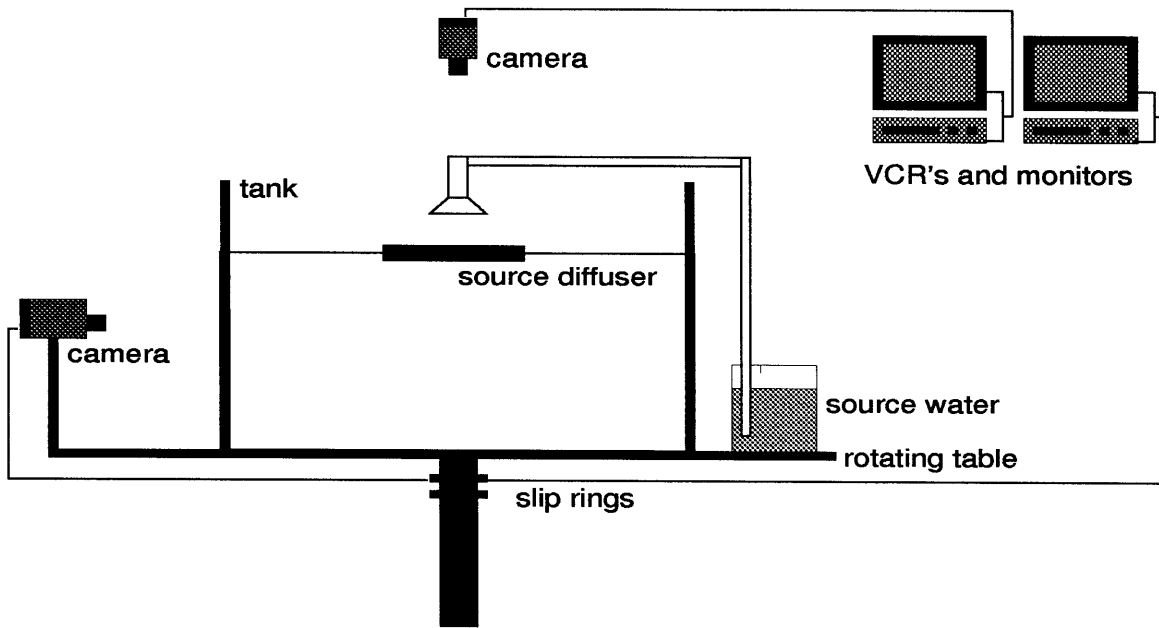
Figure 3.1: A side view schematic of the laboratory apparatus used for this study.

through a diffuser on the bottom covered with an inch of gravel. This helps maintain solid-body rotation. The tank is filled to 30 cm above the gravel.

The dense water introduced at the surface is marked with neutrally buoyant blue dye to facilitate flow visualization. The first source used was a paint sprayer; the configuration is depicted in Figure 3.2. The sprayer is housed in a plastic cage which serves several purposes. The cage permits mist to fall only on the desired patch and catches any drips which accumulate on the sides (ensuring spatial uniformity of coverage). The cage also halts any wind generated by the paint sprayer, preventing the transfer of momentum to or evaporative cooling from the surface. The paint sprayer generates a fine-enough mist to satisfy the uniformity and zero momentum criterion.

The second source used allows a larger area to be affected. This source is a variation on that used by [Maxworthy and Narimousa, 1994]. A hard plastic cylinder of the desired diameter is used. The bottom is covered with a layer of mesh topped
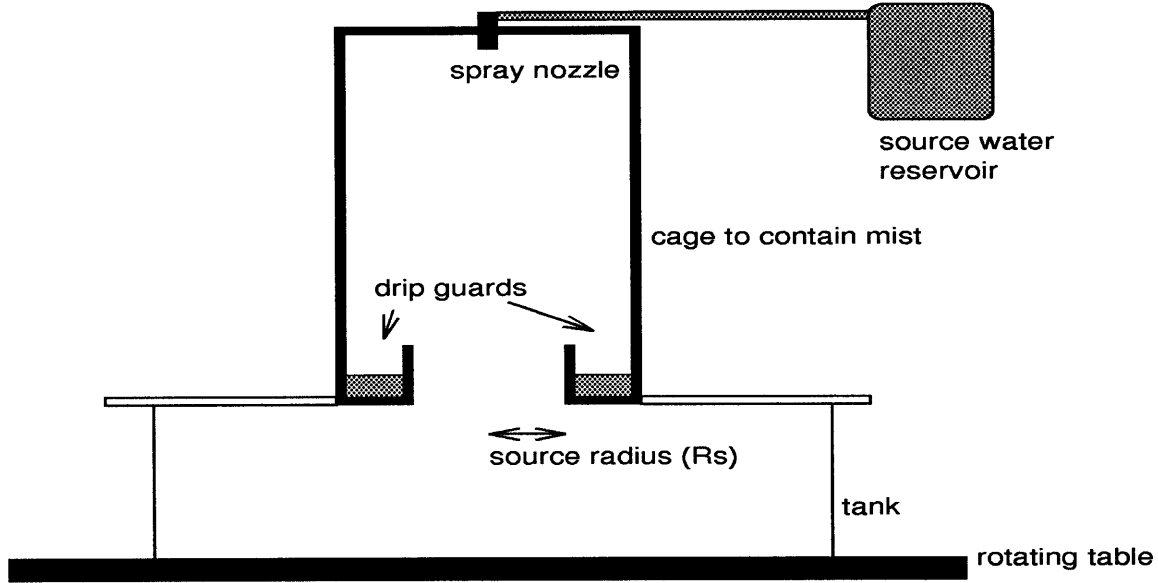
Figure 3.2: A schematic of the paint sprayer used to introduce dense water to the experiments discussed here.

by a layer of filter paper, topped by a layer of sponge. Dense fluid is introduced to this diffuser via a small tube leading from a reservoir.

The laboratory procedure begins with the tank rotating. It is filled from the bottom with a stratified fluid and left undisturbed until it has reached solid body rotation (this is approximately 2 hours). When this is established the experiment begins with the initiation of the buoyancy flux. The resulting flow is recorded using the video cameras. Surface currents are marked with passive drifters. The experiment terminates when the flow reaches a side wall. In some instances it was necessary to terminate the laboratory experiment sooner due to a practical problem with the paint sprayer source. To prevent salt build-up in the electronics of the laboratory, the paint spray source is always discontinued after 60-70 s.

Salt is used, rather than temperature, to induce stratification and buoyancy loss. This eliminates many practical laboratory problems including: secondary convection during filling and run; unwanted circulation due to the temperature gradient between the center of the tank and the side walls; and unmeasurable buoyancy loss

28

due to uncontrolled evaporation. Salt diffuses one hundred times more slowly than heat and hence a salt anomaly is easier to manipulate than a temperature anomaly. However, it was not possible to make the paint spray cage completely air tight so salt mist eventually escapes into the laboratory.

3.2 Measurement and qualitative results

The laboratory experiments were set up primarily to explore the widest possible range of N, f, and R_s. This distribution of experimental parameters facilitates the investigation of the scalings l_{eddy}^{scal} and d_{final}^{scal} presented in Chapter 2. Table 3.1 lists the experimental parameters used in each run. Also displayed are the non-dimensional numbers N/f, R_o^*, and R_s/H. In all cases $H = 30$ cm was the total depth of the fluid in the laboratory tank. The first set of runs were performed with a constant value of $R_s = 15$ cm, values of N ranging from $0.2 < N < 0.9$ $/s$ and values of f ranging from $0.125 < f < 0.5$ $/s$. The second set of experiments were performed varying the value of R_s between $7.5 < R_s < 22.5$ cm, again varying N and f.

The properties measured in the laboratory are the mode number of the baroclinic instability (M^{lab}), length scale of the baroclinic eddies (l_{eddy}^{lab}), the associated maximum velocity (u_{rim}^{lab}), and the final depth of convective penetration, (d_{max}^{lab}). The mode number is measured in the laboratory by observing the shape of the chimney from above once eddies are fully formed. Figure 3.3 (a) shows the addition of source water through the plexi-glass diffuser, as seen from above. Immediately one sees one drawback in the laboratory set-up: no data can be taken from the area directly beneath the source. It is impossible to trace velocities when the source is obscuring the view. In the case of the plexi-glass source, this area is obscured for the duration of the experiment. In the case of the paint spray source, the entire surface of the tank is obscured, but only up until the source is switched off at 60-70 s. Thereafter, the cage is removed offering an unimpeded view of the surface flow.

Lab run	$f(1/s)$	$N(1/s)$	R_s (cm)	N/f	R_o^*	R_s/H $(H = 30cm)$
1	0.500	.82	15	1.64	.05	0.50
2	0.500	.45	15	0.90	.05	0.50
3	0.500	.20	15	0.40	.05	0.50
4	0.250	.83	15	3.31	.15	0.50
5	0.250	.41	15	1.65	.15	0.50
6	0.250	.22	15	0.88	.15	0.50
7	0.125	.83	15	6.64	.41	0.50
8	0.125	.45	15	3.28	.41	0.50
9	0.125	.24	15	1.92	.41	0.50
10	0.500	.8	7.5	1.60	.05	0.25
11	0.500	.38	7.5	0.76	.05	0.25
12	0.500	.29	7.5	0.58	.05	0.25
13	0.250	.86	7.5	3.44	.15	0.25
14	0.250	.4	7.5	1.60	.15	0.25
15	0.250	.22	7.5	0.88	.15	0.25
16	0.500	.36	15	0.72	.04	0.50
17	0.250	.4	15	1.60	.11	0.50
18	0.250	.37	15	1.48	.31	0.50
19	0.125	.38	15	3.04	.41	0.50
20	0.500	.43	22.5	0.86	.04	0.75
21	0.250	.34	22.5	1.36	.11	0.75
22	0.250	.44	22.5	1.76	.31	0.75
23	0.125	.44	22.5	3.52	.41	0.75

Table 3.1: This table displays the experimental parameters for the laboratory experiments reported here. Also shown are the values of the significant non-dimensional parameters. The first 9 experiments listed are those used in comparison with the numerical estimates. The rest are used to further test the scaling theory for d_{final}^{scal}.
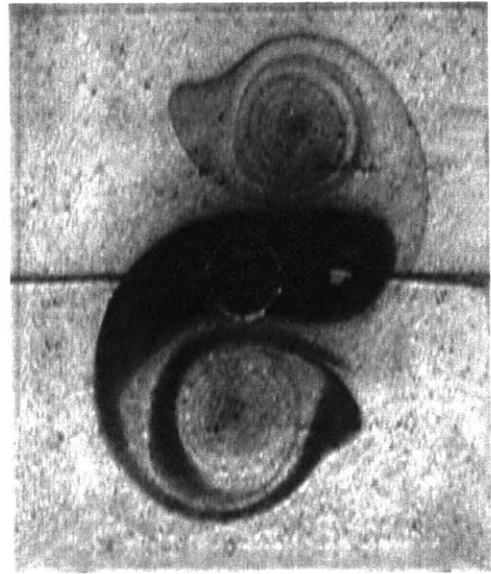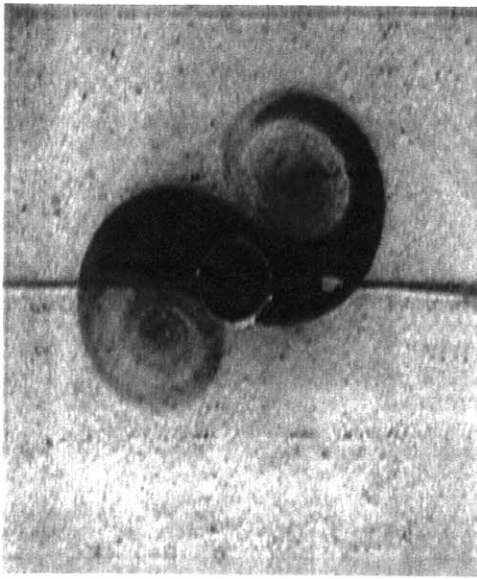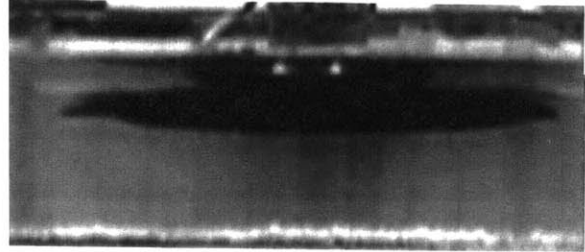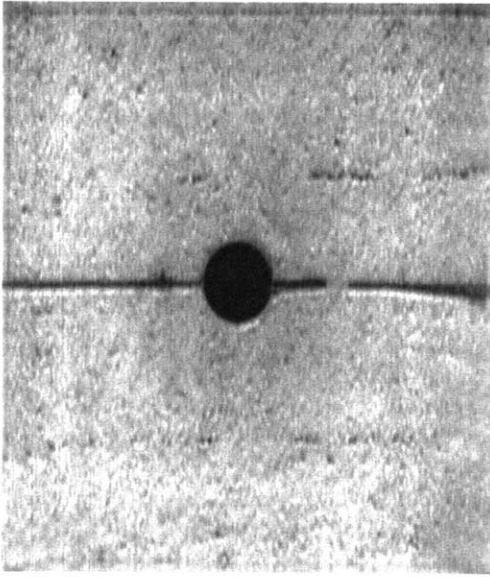
Figure 3.3: Photographs of the laboratory experiment: a) overhead view of laboratory experiment at start, note the dyed water just becoming apparent at edges of source, and reservoir of dyed fluid present in the source diffuser; b) side view of the laboratory experiment, note the narrow chimney beneath the source, and the spreading of the dyed fluid at depth; c) overhead view of laboratory experiment, two distinct eddies have formed and are propagating away from the source; d) again from overhead, now the anti-cyclonic circulation is accreting dyed water from the cyclonic eddy.

31

Once the dense chimney fluid reaches its neutrally buoyant depth, it begins to spread out from under the source and becomes visible from the above. The horizontal extent of the spreading is evident in the cross section photograph displayed in Figure 3.3 (b). The chimney breaks into a discrete number of eddies which migrate away from the source. In many instances, new eddies seen from above form under the source when the first eddies drift away. The number of eddies being simultaneously shed by the chimney is identified as the mode number. As discussed above, the initial mode number that appears in the experiment decreases, as the chimney penetrates deeper, the visible effect being a coalescence of eddies. Figure 3.3 (c) shows two well developed eddies propagating away from the source. They are each still attached to the source water through a narrow filament. The following panel shows the two eddies at a later time when some of the dye is being advected around into the anti-cyclone.

Recall that Figure 1.8 showed a high mode instability, illustrating a surface manifestation of the sub-surface anti-cyclone. The surface cyclone and sub-surface anti-cyclone always propagate together as a pair. In some high mode parameter regimes there is an apparent lateral separation of the two circulations and the anti-cyclone has sufficient strength to be perceptible at the surface. This is discussed further in Appendix I. The surface cyclone often extends to depth. In Figure 1.8 the lateral separation is marked by the accretion of dye from the cyclone into the anti-cyclone. There is frequently some ambiguity in determining mode number (M^{lab}). A half-formed eddy may be produced, for example, or there may be four distinct waves present, but only three eddies shed due to coalescence. The measurement uncertainty for mode number is then ± 1.

Our working definition of the length scale of the eddies (l^{lab}_{eddy}) is the average diameter of all eddies present. These measurements were taken over a one minute interval beginning approximately 100 s after the start of the experiment. The laboratory method of measurement may be a consistent underestimate. The eddies must necessarily be seen with the aid of the source dye. It is clear that the dye cannot be

transported beyond the limits of the circulation. However, it is not clear that visible amounts of dye reach to the extent of the circulation. It is possible that the velocity field extends beyond the region of tracer mixing. This is a systematic error and so will not affect the analysis of trends in the laboratory data, but it may be important when comparing the laboratory and numerical data. There is an uncertainty associated with the method of measuring the eddy lengths. This uncertainty comes from parallax involved in measuring the eddies on the monitor screen instead of in the tank, and with the resolution of the picture. The measurements are good to ± 3 cm.

The maximum surface velocities (u_{rim}^{lab}) were recorded at the same time as the eddy sizes. These velocities do not represent the maximum velocities which are present in the tank during the experiment, because velocities continue to increase throughout the duration of the experiment. In the laboratory the maximum velocities were measured at around 100 s by tracking surface tracers for $3 - 4$ s. Sub-surface velocities could not be measured.

These speed estimates may be underestimates for two reasons. It is likely that no surface tracer was present where the velocity had its maximum. Since a number of particles were tracked, it is safe to assume that the real maximum is not far removed from the maximum tracer velocities, but it may be larger. It is also possible that the tracers themselves introduced some drag, so that the velocities measured might again be expected to be lower than the actual maximum. The measurement of velocities in the laboratory by tracking the tracers on the monitor screen can only be good to within 50% uncertainty.

It is possible to visualize the shear set up by the opposing circulations at the surface and at depth. A permanganate crystal dropped at the surface will leave a vertical line of dye as it descends. In the region of the source the upper extent of such a line was observed to move clockwise with the rotation of the tank, while the lower portion of the line is carried counterclockwise away from it. From this observed

shear an opposing circulation is inferred with cyclonic circulation at the surface and anti-cyclonic circulation at depth.

The final depth of the convectively produced mixed layer (d^{lab}_{max}) was recorded by eye with a meter stick held to the side of the tank during the experiment. Figure 3.3 (c) shows a side view of convective overturning over the entire horizontal extent of the source. The deepest point of the dye interface was chosen as d^{lab}_{max}. This does not represent the average resting depth of the convectively produced water. Instead, it represents the maximum depth to which the convection had an influence. As will be seen below in 4.3, this is important for comparing the laboratory and numerical data. The measurement uncertainty associated with d^{lab}_{max} is ± 1.5 cm; estimated from the complications of parallax in measuring something in the center of the tank from the side, and the ambiguity of the dye interface.

3.3 Results

Measurements were made of mode number, maximum horizontal speed, eddy length and maximum depth in the laboratory for comparison with our numerical data and to interpret in the context of our scaling laws. In addition, several more laboratory experiments were performed to further investigate d^{scal}_{final}. The laboratory data for comparison with the numerical data is presented in Table 3.2; the actual comparison is discussed in section 4.3. Tables 3.3 and 3.4 show the d^{lab}_{max} data from the supplemental experiments. The set of laboratory and numerical experiments performed for comparison have B_o fixed at .3 cm^2/s^3 and $R_s = 15$ cm. The supplemental experiments were carried out with $R_s = 7.5 - 22.5$ cm, to further examine the dependence of depth on R_s.

Figures 3.4 - 3.11 show the measured values of M^{lab}, U^{lab}_{Rim}, l^{lab}_{eddy} and d^{lab}_{max}. The x axis is the non-dimensional number N/f in Figures 3.4, 3.6, 3.8 and 3.10, and R^*_o in Figures 3.5, 3.7, 3.9 and 3.11. The y axis is the ratio of the observed to the theoretical

34

Experiment	1	2	3	4	5	6	7	8	9
$N(1/s)$	0.82	0.45	0.20	0.82	0.41	0.22	0.83	0.41	0.24
$f(1/s)$	0.50	0.50	0.50	0.25	0.25	0.25	0.1250	0.1250	0.1250
M	3	3	4	3	2	3	2	1	2
$V_{eddy}(cm/s)$	0.90	1.40	1.30	1.10	1.50	1.50	2.10	1.60	2.10
$L_{eddy}(cm)$	8.00	7.40	7.60	16.70	16.00	17.70	25.00	32.00	29.50
$d_{final}(cm)$	6.00	11./16.	23.00	7.50	12.25/15./21	27.00	10.20	13.50/18.	27.00

Table 3.2: Laboratory results for comparison with the numerical data.

N

f	0.8	0.4	0.2
0.500	4.5000	9.0000	17.00
0.250	4.00	8.0000	18.00
0.125	-	-	-

Table 3.3: Laboratory values for maximum depth, $R_s = 7.5$ cm.

N

f	0.8	0.4	0.2
0.500	-	17.00	-
0.250	-	17.00—18.00	-
0.125	-	17.00	-

Table 3.4: Laboratory values for maximum depth, $R_s = 7.5$ cm.

prediction. The uncertainty in measuring the observed quantity must also be scaled by the same theoretical prediction. Even for those cases in which the measurement uncertainty is fixed, the predicted value varies from point to point, therefore the scaled deviation varies as well. There is no significant error associated with the theoretical prediction. The figures display a weighted linear regression between the non-dimensional numbers and the observations normalized by their predicted values. Only the average of the scaled uncertainty is displayed as an error bar in each figure. The straight line displayed is the fit to the data. The dotted lines represent the 95 % confidence limits associated with the fit. The variance of the fit is calculated as a propagation of the variances of the estimated slope and intercept, so that $\sigma_{fit}^2 = \sqrt{\sigma_\alpha^2 x^2 + \sigma_\beta^2}$. The dotted lines are calculated as the fit $\pm 1.96\sqrt{\sigma_{fit}^2}$.

The non-dimensional number $\frac{observation}{prediction}$ does not introduce any new parameters to the system, therefore it must be a linear combination of the three non-dimensional numbers with which we have chosen to describe the system. If the prediction is an accurate representation of the dependence of observation on system parameters, then there will be no dependence of $\frac{observation}{prediction}$ on any of the non-dimensional numbers. For any plot of $\frac{observation}{prediction}$ vs non-dimensional number there would be no trend, ie. $\alpha = 0$. The intercept is the constant of proportionality between the observations and the predicted scalings. If the intercept is unity then all of the parameters we are looking at have been accurately portrayed in the predicted scaling.

The calculated values of slope, (α) and intercept, (β) are shown in Table 3.5, along with their respective variances (σ_α^2 and σ_β^2). These values are plotted in Figures 3.4 - 3.11. Also tabulated are the 95% confidence limits for the slope. Figure 3.4 shows $\frac{M^{lab}}{M^{scal}}$ plotted against N/f, and Figure 3.5 shows $\frac{M^{lab}}{M^{scal}}$ versus R_o^*. The scaling used here comes from the prediction $M^{scal} = \frac{\sqrt{8}(R_o^*)^2 f}{Nh}$ calculated using $h = d_{final}^{scal} = \frac{(R_s B_o)^{1/3}}{N}$. Recall that d_{final} cannot be measured in the laboratory, only the quantity d_{max}^{lab} is obtained.

comparison	α	β	σ_α^2	σ_β^2	$\alpha + \epsilon$	$\alpha - \epsilon$
$\frac{d_{max}^{lab}}{d_{final}^{scal}}$ vs N/f	0.3605	3.1023	0.0053	0.0152	0.5033	0.2177
$\frac{d_{max}^{lab}}{d_{final}^{scal}}$ vs R_o^*	2.1213	3.2565	0.3292	0.0137	3.2458	0.9968
$\frac{M^{lab}}{M^{scal}}$ vs N/f	0.0323	0.3204	0.0016	0.0041	0.1101	-0.0455
$\frac{M^{lab}}{M^{scal}}$ vs R_o^*	0.7086	0.3028	0.2584	0.0033	1.7049	-0.2877
$\frac{u_{rim}^{lab}}{u_{rim}^{scal}}$ vs N/f	-0.0390	0.9900	0.0081	0.0757	0.1377	-0.2156
$\frac{u_{rim}^{lab}}{u_{rim}^{scal}}$ vs R_o^*	-0.2900	0.9546	0.9879	0.0708	1.6581	-2.2380
$\frac{l_{eddy}^{lab}}{l_{eddy}^{scal}}$ vs N/f	-0.0948	2.5842	0.0032	0.0505	0.0159	-0.2055
$\frac{l_{eddy}^{lab}}{l_{eddy}^{scal}}$ vs R_o^*	-1.0299	2.6149	0.8646	0.1160	0.7925	-2.8524

Table 3.5: Parameter estimates for least squares fit to the data. Observational data was divided by scaling prediction, the resulting value was compared to the non-dimensional numbers N/f and R_o^*. Shown here are the estimates of the slope, α, the intercept, β, and their associated variance, σ_α^2 and σ_β^2, and the confidence intervals on the slope estimate $\alpha \pm \epsilon$ where $\epsilon = 1.97 \times \sigma_\alpha$, 95% confidence. These quantities are discussed further in the text.

The constant of proportionality between the observations and predicted scaling for the case of N/f is 0.3204 and for the case of R_o^* is 0.3028. As we will see in the following chapter, the discrepancy between these constants and unity can be explained by a missing constant in the prediction for d_{final}^{scal}, which will be shown empirically in section 4.4 to be ≈ 2.3. When the missing constant of proportionality is included, the constants are ≈ 0.74 and 0.70. In both cases a zero slope lies within the 95% confidence limits.

Figure 3.6 shows the observations of maximum horizontal speed $\frac{u_{rim}^{lab}}{u_{rim}^{scal}}$, against N/f, Figure 3.7 shows the same quantity against R_o^*. The scaling is calculated directly from our equation

$$u_{rim}^{scal} = Nh \sim \sqrt{2B_o/f}.$$

The value $u^{lab} = 0.9900 u^{scal}$ for the comparison with N/f and $u^{lab} = 0.9546 u^{scal}$ in the comparison with R_o^*. Again the zero slope lies within the confidence limits,
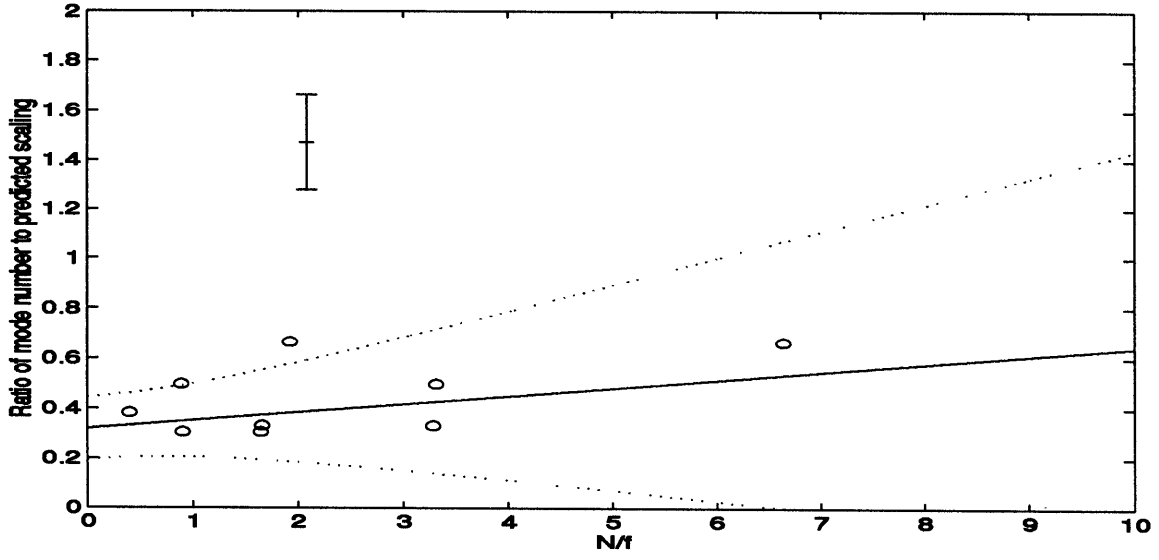
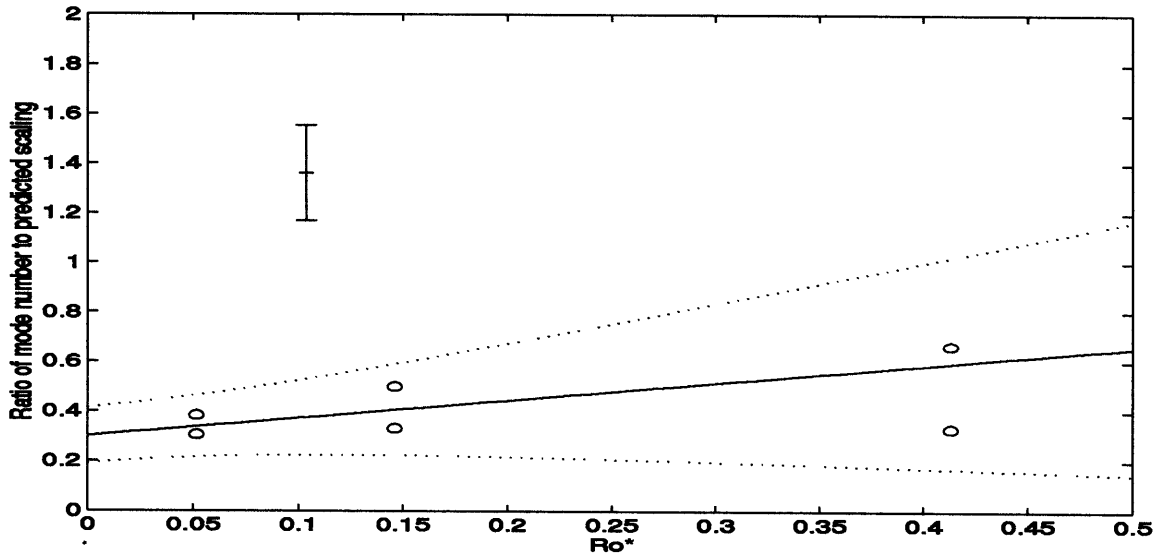Figure 3.4: Laboratory values for normalized mode number $\left(\frac{M^{lab}}{M^{scal}}\right)$ plotted against N/f.

Figure 3.5: Laboratory values for normalized mode number $\left(\frac{M^{lab}}{M^{scal}}\right)$ plotted against R_o^*.
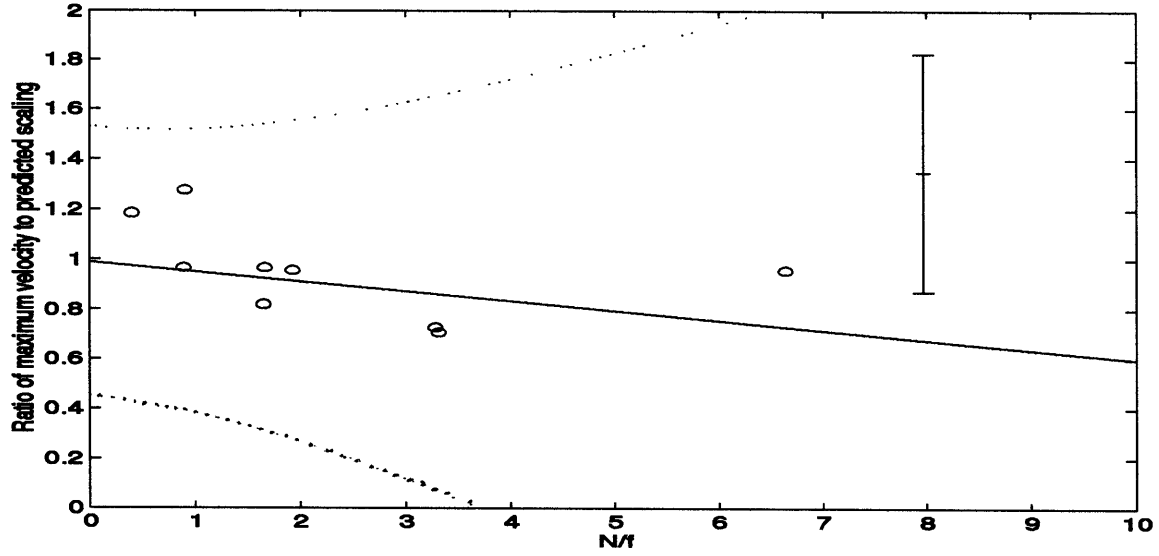
Figure 3.6: Laboratory values for normalized maximum velocity ($\frac{u_{rim}^{lab}}{u_{rim}^{scal}}$) plotted against N/f.

indicating that our predicted scaling accurately describes the dependence of u_{rim} on the experimental parameters.

The next case is l_{eddy}. Figure 3.8 shows the scaled observations of $\frac{l_{eddy}^{lab}}{l_{eddy}^{scal}}$ versus N/f, Figure 3.9 shows the same quantity versus R_o^*. The scaling used comes from choosing the predicted value of d_{final} for h in our equation

$$l_{eddy}^{scal} = \frac{Nh}{f}.$$

The value $l_{eddy}^{lab} = 2.5842 l_{eddy}^{scal}$ for the comparison with N/f and $l_{eddy}^{lab} = 2.6149 l_{eddy}^{scal}$ in the comparison with R_o^*. The resulting constants of proportionality are 2.5842 and 2.6149. The discrepancy between these and unity can be completely explained again by the factor of 2.3 associated with d_{final}. The corrected values are ≈ 1.123 and 1.136. In both cases zero slope lies within the confidence limits.

The last case is d_{max}. Figure 3.10 shows $\frac{d_{max}^{lab}}{d_{final}^{scal}}$ versus N/f, while Figure 3.11 shows the same quantity versus R_o^*. In neither case does the zero slope lie within the confidence limits. This suggests that the laboratory measurement of d_{max}^{lab} is not accurately described by the prediction for d_{final}^{scal}.

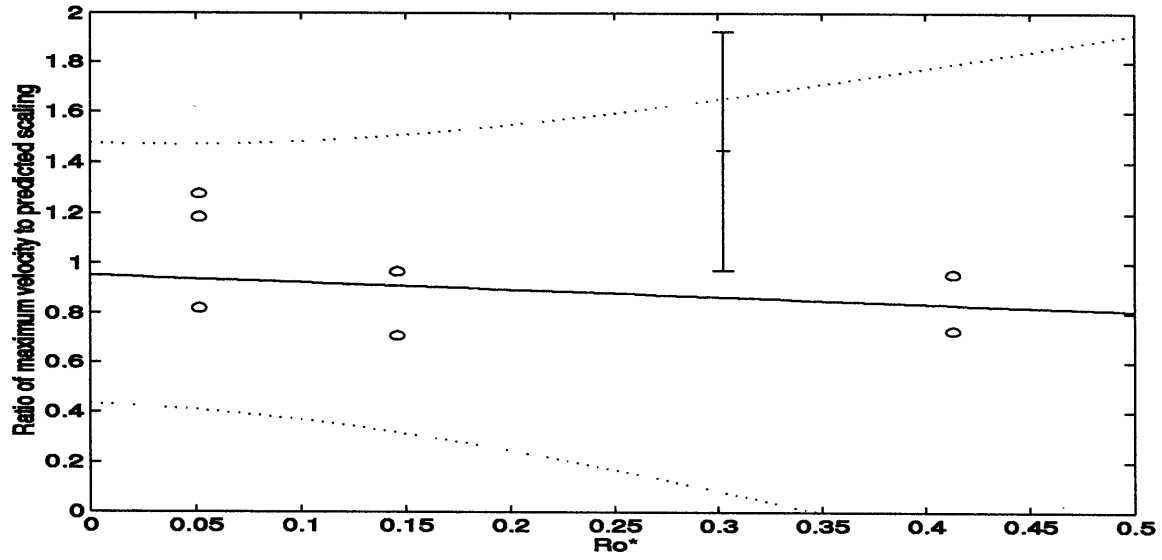Figure 3.7: Laboratory values for normalized maximum velocity $\left(\frac{u_{rim}^{lab}}{u_{rim}^{scal}}\right)$ plotted against R_o^*.
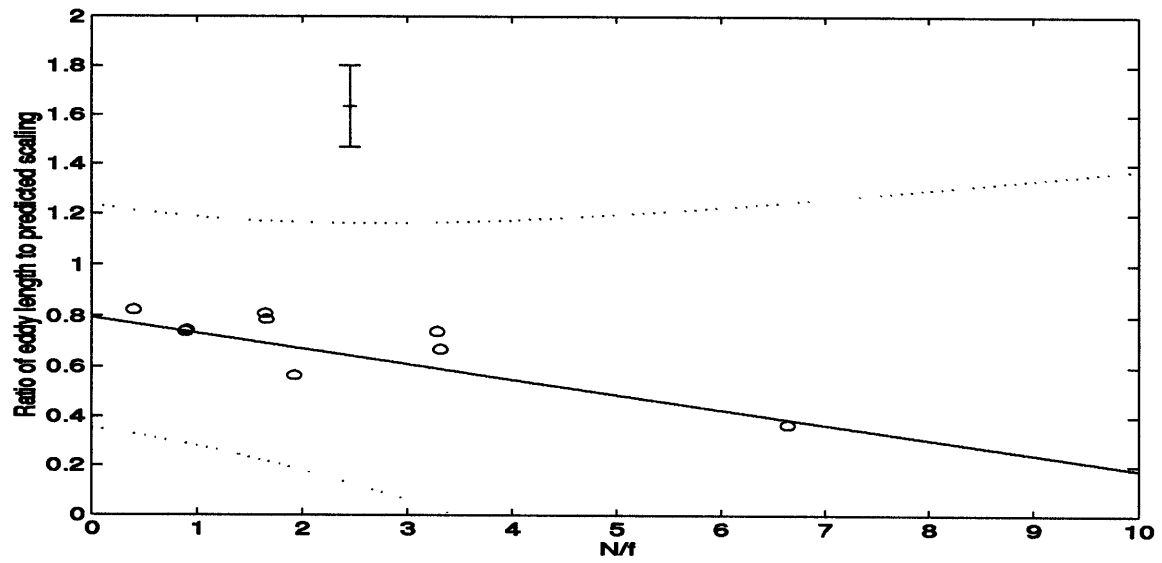
Figure 3.8: Laboratory values for normalized eddy length $\left(\frac{l_{eddy}^{lab}}{l_{eddy}^{scal}}\right)$ plotted against N/f.

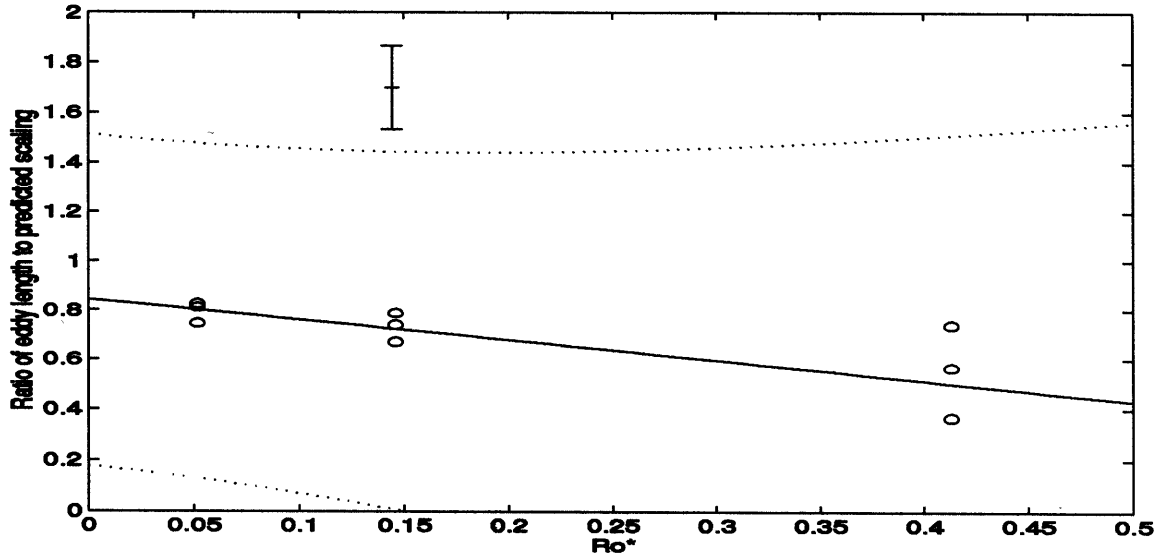Figure 3.9: Laboratory values for normalized eddy length $\left(\frac{l_{eddy}^{lab}}{l_{eddy}^{scal}}\right)$ plotted against R_o^*.
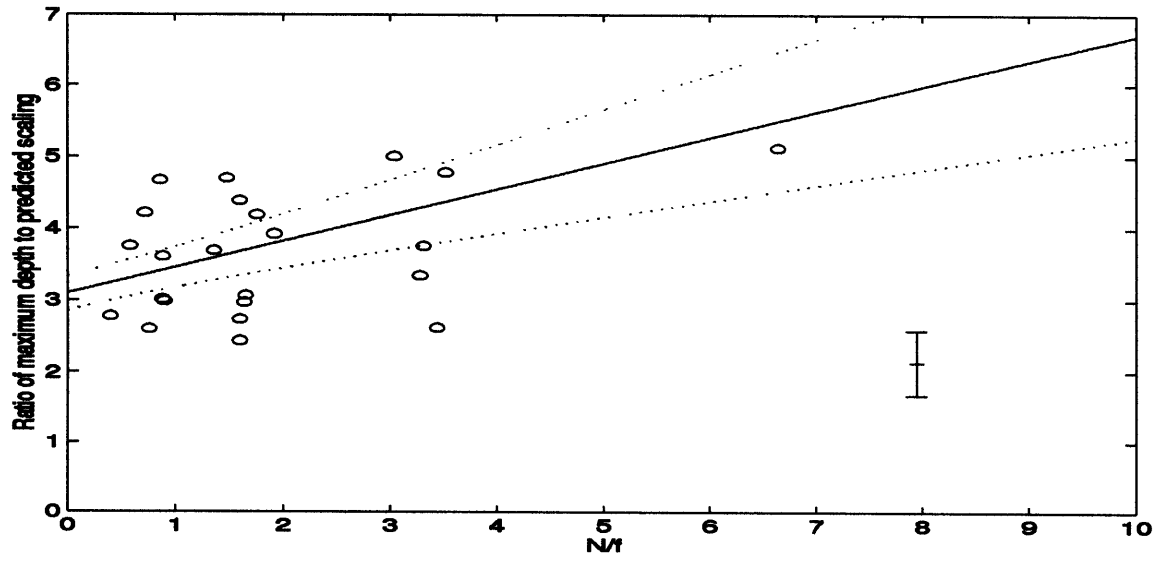

Figure 3.10: Laboratory values for normalized maximum depth $\left(\frac{d_{max}^{lab}}{d_{final}^{scal}}\right)$ plotted against N/f.
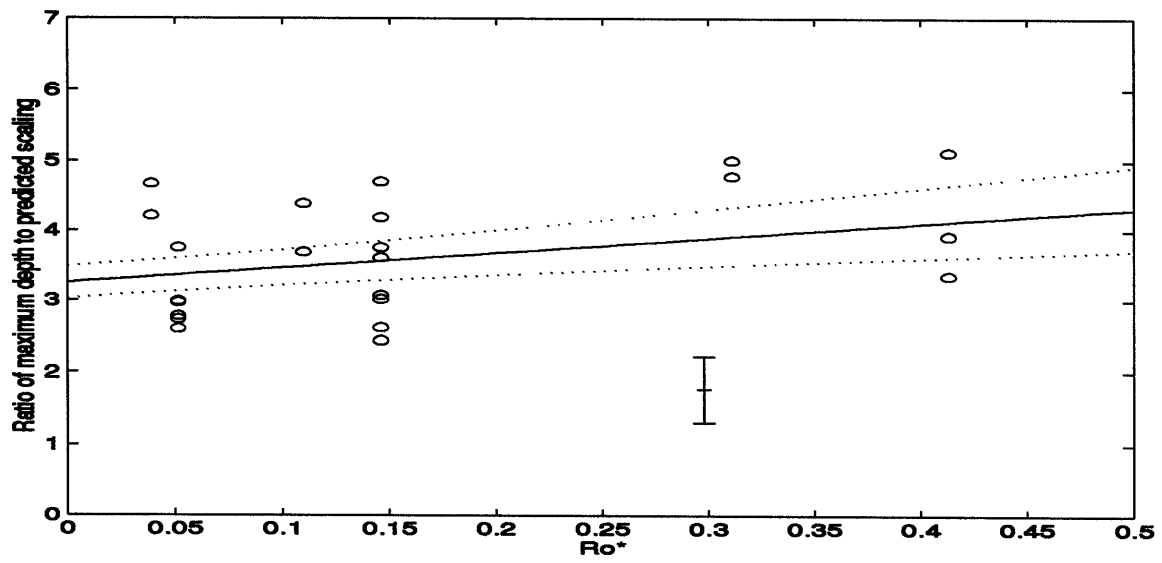
41

Figure 3.11: Laboratory values for normalized maximum depth $\left(\frac{d_{max}^{lab}}{d_{final}^{scal}}\right)$ plotted against R_o^*.

Chapter 4

The Computational Analog

4.1 Numerical parameters

The numerical model used in this study is the non-hydrostatic primitive equation model described in detail in [Brugge et al., 1991]. The model was developed from the atmospheric model written by Miller (1971), and adapted to become a model appropriate for studying ocean convection. The equations for a Boussinesq incompressible fluid with an equation of state appropriate for sea-water are

Momentum:

$$\frac{Du}{Df} + \frac{1}{\rho_o}\frac{\partial p'}{\partial x} - fv = v_H\left(\frac{\partial^2 u}{\partial x^2} + \frac{\partial^2 u}{\partial y^2}\right) + v_v\frac{\partial^2 u}{\partial z^2}$$

$$\frac{Dv}{Dt} + \frac{1}{\rho_o}\frac{\partial p'}{\partial y} + fu = v_H\left(\frac{\partial^2 v}{\partial x^2} + \frac{\partial^2 v}{\partial y^2}\right) + v_v\frac{\partial^2 v}{\partial z^2}$$

$$\frac{Dw}{Dt} + \frac{1}{\rho_o}\frac{\partial p'}{\partial z} + g\frac{\rho'}{\rho_o} = v_H\left(\frac{\partial^2 w}{\partial x^2} + \frac{\partial^2 w}{\partial y^2}\right) + v_v\frac{\partial^2 w}{\partial z^2}$$

43

Continuity:

$$\frac{\partial u}{\partial x} + \frac{\partial v}{\partial y} + \frac{\partial w}{\partial z} = 0$$

Density Conservation:

$$\frac{Ds}{Dt} = Q_s$$

Equation of State:

$$\rho = \rho_o(1 - \beta(s - s_o))$$

Where:

$$\frac{D}{Dt} = \frac{\partial}{\partial t} + u\frac{\partial}{\partial x} + v\frac{\partial}{\partial y} + w\frac{\partial}{\partial z} \qquad \text{in height coordinates.}$$

Here u, v and w are the customary velocities in the x, y and z directions, Q_s is equivalent salt flux, ρ is density, p is pressure, and ν_H and ν_V are the horizontal and vertical coefficients of diffusion respectively.

The full equation of state $\rho = \rho\,(\text{T,S,}z)$ is not required in the parameter regime of the laboratory as pressure will never be significant in the range of 30-40 cm depth, and temperature never varies from 21 °C.

In these equations ρ' is the perturbation of the density field from its initial (reference) state ρ_s; ρ_o is a standard constant value. Similarly, p' is the deviation of pressure from the initial hydrostatically balanced p_s.

The model is doubly periodic and has a rigid lid and free-slip bottom. For practical purposes this means that there is no side wall interference until a migrating eddy leaves the domain to one side and re-enters from the other side. There will be no bottom drag to consider. The rigid lid also ensures that there are no surface gravity wave modes to cause numerical problems.

A time step of 0.1 s is used to satisfy the CFL conditions with grid spacing of only 0.86 and 1.56 cm in the horizontal and vertical respectively.

44

The buoyancy forcing is applied over a circular patch of desired radius. Effectively the model introduces salt to the appropriate disk of water, one grid space deep. There is no addition of volume to the system, only salt.

The physical values of kinematic diffusivity were used in the model $\nu = 10^{-6} \ m^2/s$. The molecular diffusion coefficients for salt in water were adjusted in keeping with stability criteria. Instead of the molecular value $\kappa_s = 10^{-9} \ m^2/s$, the model was initiated with $\kappa_v = \kappa_h = 10^{-6} \ m^2/s$, where κ_v and κ_h are the vertical and horizontal diffusion coefficients respectively.

4.2   Measurement and qualitative results

The numerical experiments were set up to first duplicate the laboratory experiments and then expand the ranges of N, f, and R_s beyond the capabilities of the laboratory. Table 4.1 lists the experimental parameters for each run. Also displayed are the non-dimensional numbers N/f, R_o^*, and R_s/H, where H is again 30 cm and is the total depth of the numerical tank. The first set of runs was performed with a constant value of $R_s = 15 \ cm$, values of N ranging from $0.18 < N < 0.9 \ /s$ and values of f ranging from $0.125 < f < 1.0 \ /s$. The second set of experiments were performed varying the value of R_s from $7.5 < R_S < 22.5 \ cm$, while keeping constant values of $N \approx 0.4 \ /s$ and $f = 0.25 \ /s$.

The values measured in the numerical work are mode number of the baroclinic instability (M^{num}), length scale of the baroclinic eddies (l_{eddy}^{num}), maximum velocity (u_{rim}^{num}), final resting depth of the convectively produced water (d_{final}^{num}), maximum depth of convective influence for comparison with the laboratory (d_{max}^{num}), and final volume of convectively produced water (V_{final}^{num}).

Mode number (M^{num}) is measured in the computations the same way it is measured in the laboratory. However, instead of the dye field, the velocity field is used. For future experiments it would be possible to advect a passive tracer in the

Comp run	f	N	R_s (cm)	N/f	R_o^*	R_s/H (H=30cm)
1	0.5000	0.9370	7.5	1.8740	0.0516	0.25
2	0.5000	0.4310	7.5	0.8620	0.0516	0.25
3	0.5000	0.2400	7.5	0.4800	0.0516	0.25
4	0.2500	0.9370	7.5	3.7480	0.1461	0.25
5	0.2500	0.4310	7.5	1.7240	0.1461	0.25
6	0.2500	0.2400	7.5	0.9600	0.1461	0.25
7	0.1250	0.9370	7.5	7.4960	0.4131	0.25
8	0.1250	0.4310	7.5	3.4480	0.4131	0.25
9	0.1250	0.2400	7.5	1.9200	0.4131	0.25
10	0.5000	0.9370	15.0	1.8740	0.0516	0.50
11	0.5000	0.4310	15.0	0.8620	0.0516	0.50
12	0.5000	0.2400	15.0	0.4800	0.0516	0.50
13	0.2500	0.9370	15.0	3.7480	0.1461	0.50
14	0.2500	0.4310	15.0	1.7240	0.1461	0.50
15	0.2500	0.2400	15.0	0.9600	0.1461	0.50
16	0.1250	0.9370	15.0	7.4960	0.4131	0.50
17	0.1250	0.4310	15.0	3.4480	0.4131	0.50
18	0.1250	0.2400	15.0	1.9200	0.4131	0.50
19	0.2500	0.1800	15.0	0.7200	0.1461	0.50
20	1.0000	0.2400	15.0	0.2400	0.0183	0.50
21	0.2500	0.4310	22.5	1.7240	0.1461	0.75
22	0.5000	0.4310	22.5	0.8620	0.0516	0.75
23	0.1250	0.4310	22.5	3.4480	0.4131	0.75

Table 4.1: This table displays the experimental parameters for the numerical experiments. Also shown are the values of the significant non-dimensional parameters.

numerical experiments. Figure 4.1 (a) shows an unobscured overhead view of the velocity field at the beginning of an experiment, after the forcing has been initiated. The plot shown is a horizontal cross section at level 2 in the model, the level at the bottom of the source block. Figure 4.1 (b) shows a side view of the experiment; the picture displays a cross section through the center of a chimney where the contours depict salt. Figure 4.1 (c) shows a typical mode three instability, displaying several well developed eddies propagating away from the source. Figure 4.1 (d) shows a high mode instability, illustrating the surface manifestation of the sub-surface anti-cyclone. The anti-cyclonic signature is discernible because of its strength and the lateral separation of the two circulations.

The length scale of the eddies (l_{eddy}^{num}) is operationally defined as the average diameter of all eddies present. These measurements were made for comparison with the laboratory data. In the numerical experiment the eddies were measured at one time only, 100 s after the start of the experiment. We have discussed above the fact that the eddies continue to grow in time. Therefore the only way to accurately compare eddies from two different experiments is to measure them at the same time. The edge of an eddy was marked by the abrupt decrease in the velocity field. As discussed above, it is possible that the velocity field extends beyond the region of tracer mixing, potentially making the numerical observations systematically larger than the laboratory observations.

The maximum surface velocities (u_{rim}^{num})were recorded at the same time as the eddy sizes, for comparison with the laboratory data. As mentioned above, the laboratory measurements may be an underestimate of the maximum velocity present. In the numerical model it is possible to locate the grid point with the maximum velocity present in the field at a given time.

The final depth of the convectively produced water (d_{final}^{num}) was recorded using information from volume histograms. The time evolution of the volume of water within a density range can give important insights into the dynamics of the convective
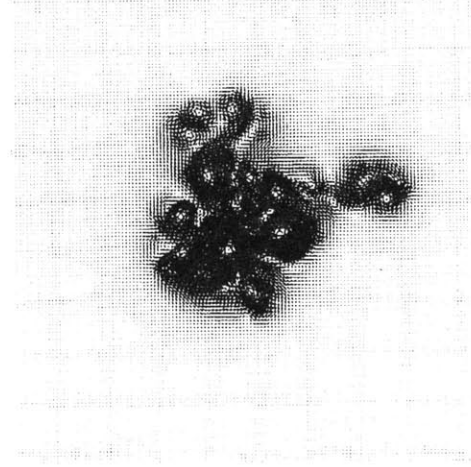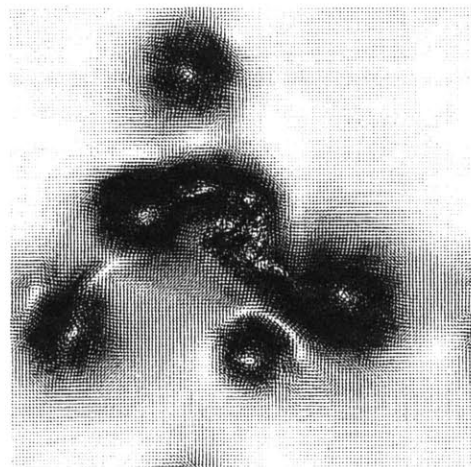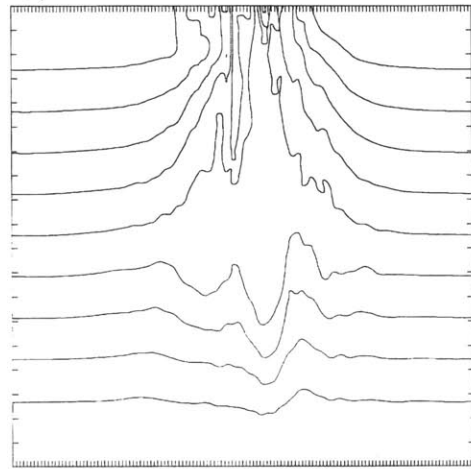
47
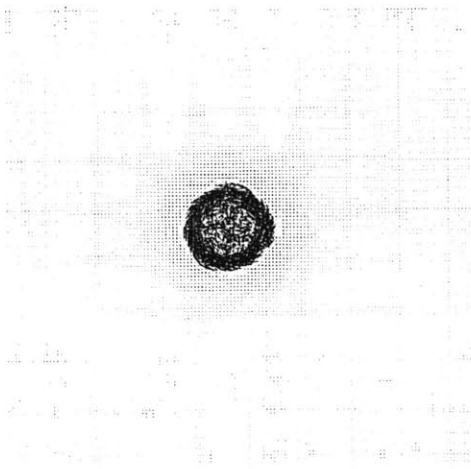
Figure 4.1: Horizontal and vertical cross sections taken from the numerical model: a) overhead view of numerical experiment at start, note the formation of individual overturning plumes; b) side view of the numerical experiment, note the narrow chimney beneath the source, and the spreading of the dense fluid at depth; c) overhead view of numerical experiment, distinct eddies have formed and are propagating away from the source; d) overhead view at surface; in this case, the anti-cyclonic circulation is apparent at the surface.

event. As discussed above, the laboratory measurement of d_{max}^{lab} gives information only on the deepest point that had contact with the convection event at any time. For the scaling arguments it is preferable to know the average resting depth of the convectively produced water. For the sake of comparison it is necessary also to measure the numerical analog to the laboratory observation, a property here assigned as d_{max}^{num}. The volume histograms are used to obtain values of d_{final}^{num}, d_{max}^{num}, and v_{final}^{num}.

Figure 4.2 illustrates the volume histogram time series. The fraction of the total volume lying within a given density range can be calculated from the salt field of the model. The value of salinity is known at every grid point for every time. If density is binned to reflect the initial stratification, then a histogram at t=0 s will show a flat line, indicating an equal amount of water in each density bin. This corresponds to the initialization of each layer in the absence of forcing. The flat line in Figure 4.2 shows 5.26% of the total volume of water in each of the 19 bins, corresponding to the 19 levels used in the model.

At t=0.1 s the buoyancy forcing is switched on. Then surface water is made more dense. As mentioned above, the buoyancy forcing in the model takes the form of added salinity, with no increase in the volume of water in the domain. The surface water is converted to denser water. This is manifest in the first peak in Figure 4.2. This line corresponds to the histogram at t=25 s. The amount of water in bins 1 and 2 has decreased, illustrating the conversion of surface water to denser water. This water shows up as a surplus in bins 3,4 and 5. The next peak corresponds to t=50 s. There is a larger surplus, now in bins 5,6 and 7. More surface water has been converted, and all of the mixed water has been subjected to more buoyancy forcing. The result is a larger mass of water at a higher density. As buoyancy forcing continues, this volume continues to increase. Note however, that the density of the convectively produced water does not continue to increase indefinitely. In every case studied the final density was achieved within the first 300 s.
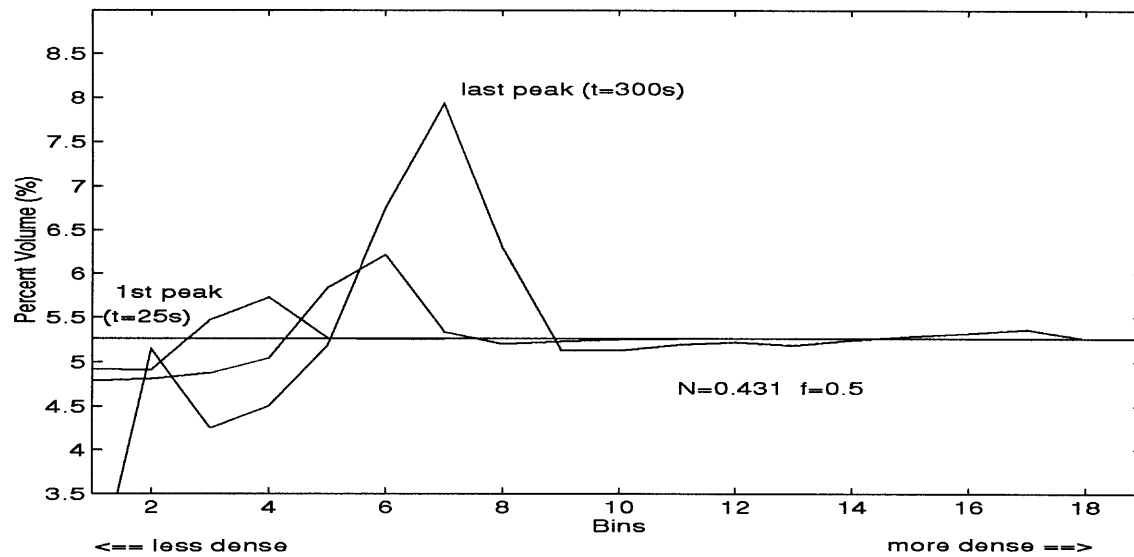
Figure 4.2: Shown here is a series of volume histograms for a typical numerical experiment. Each curve represents a histogram at a particular time, during t=0-300 s. The flat line indicates the t=0 s initial stratification with no modification to any water mass. The first peak represents t=25 s. The intermediate peak is from t=50 s. The last peak is from t=300 s. The estimates for V_{final}, d_{final} and d_{max} were all measured at this time.

Experiment	1	2	3	4	5	6	7	8	9
$N(1/s)$	0.9370	0.4310	0.24	0.9370	0.4310	0.24	0.9370	0.4310	0.24
$f(1/s)$	0.50	0.50	0.50	0.25	0.25	0.25	0.1250	0.1250	0.1250
M	5	6	4	4	4	3	2	3	2
$V_{eddy}(cm/s)$	1.71	2.66	2.48	2.14	2.41	2.79	2.83	3.00	2.83
$L_{eddy}(cm)$	15.70	14.80	10.56	-	14.76	11.87	-	-	-
$d_{max}(cm)$	7.89	14.21	18.95	7.89	14.21	18.95	7.89	14.21	17.37

Table 4.2: Numerical results for comparison with the laboratory data.

Now, several useful quantities can be defined. The depth at which water of that density would be neutrally buoyant in the background stratification is defined as the final depth of that water (d_{final}^{num}). The density of the deepest zero crossing of the convectively produced water is defined as the maximum density effected by the mode water. The depth at which water of that density would be neutrally buoyant is defined as the maximum depth of influence of the convection (d_{max}^{num}). The final volume of convectively produced water (v_{final}^{num}) is defined to be any water occupying the peak densities in excess of the original stratification. That is, the original stratification is subtracted, and an integral is performed over the dominant peak, as indicated in Figure 4.2. All of these quantities were measured at $t = 300$ s.

4.3 Comparison with the laboratory

As stated in section 3.3, laboratory measurements were made of mode number, maximum horizontal speed, eddy length and maximum depth, for comparison with the numerical data. The numerical estimates of these properties are presented in Table 4.2. Figure 4.3 shows the observed mode number, M from the laboratory plotted against the numerical estimates. The error bars in x and y indicate the measurement uncertainty associated with the numerical and laboratory estimates respectively. All of the data lie within an error bar of a one to one relationship. This indicates that the numerics are properly resolving the baroclinic instability wavelength.
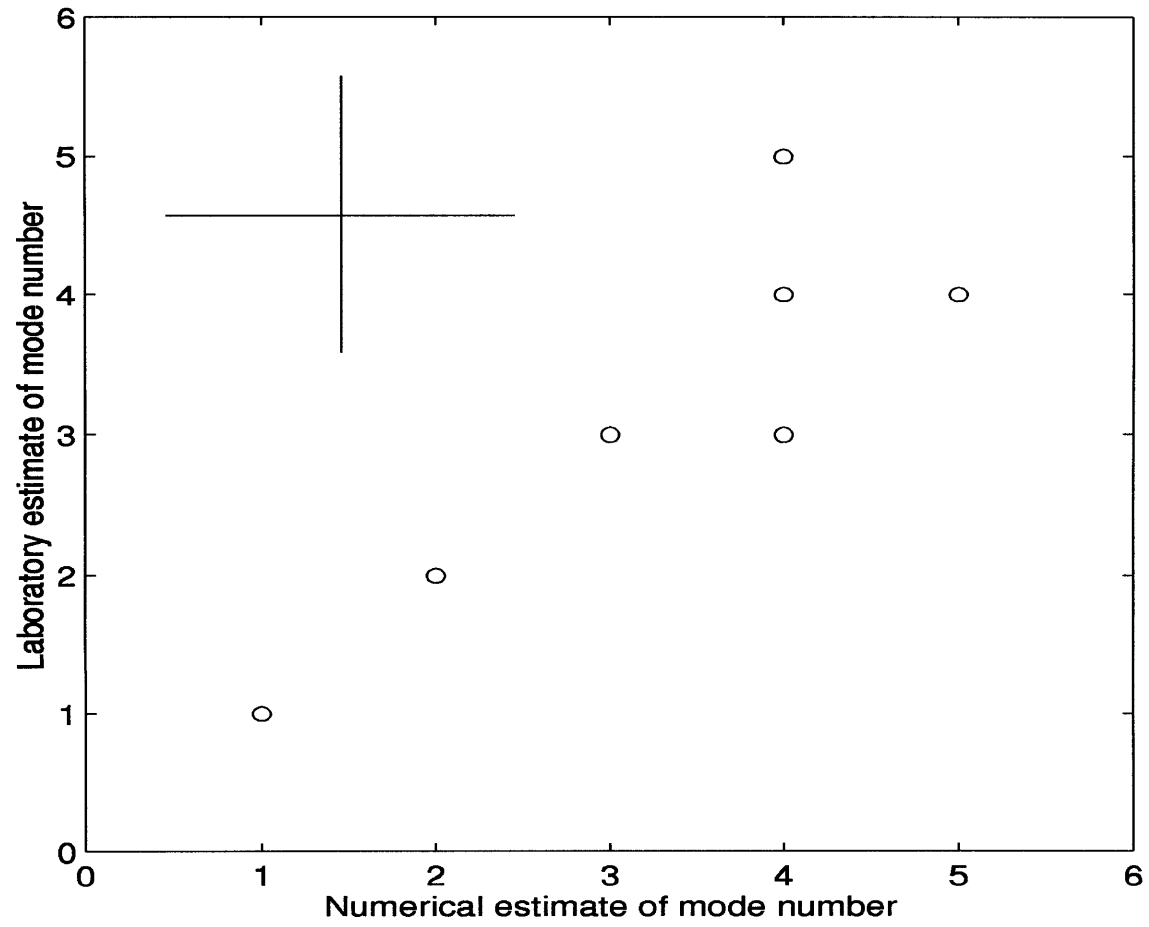
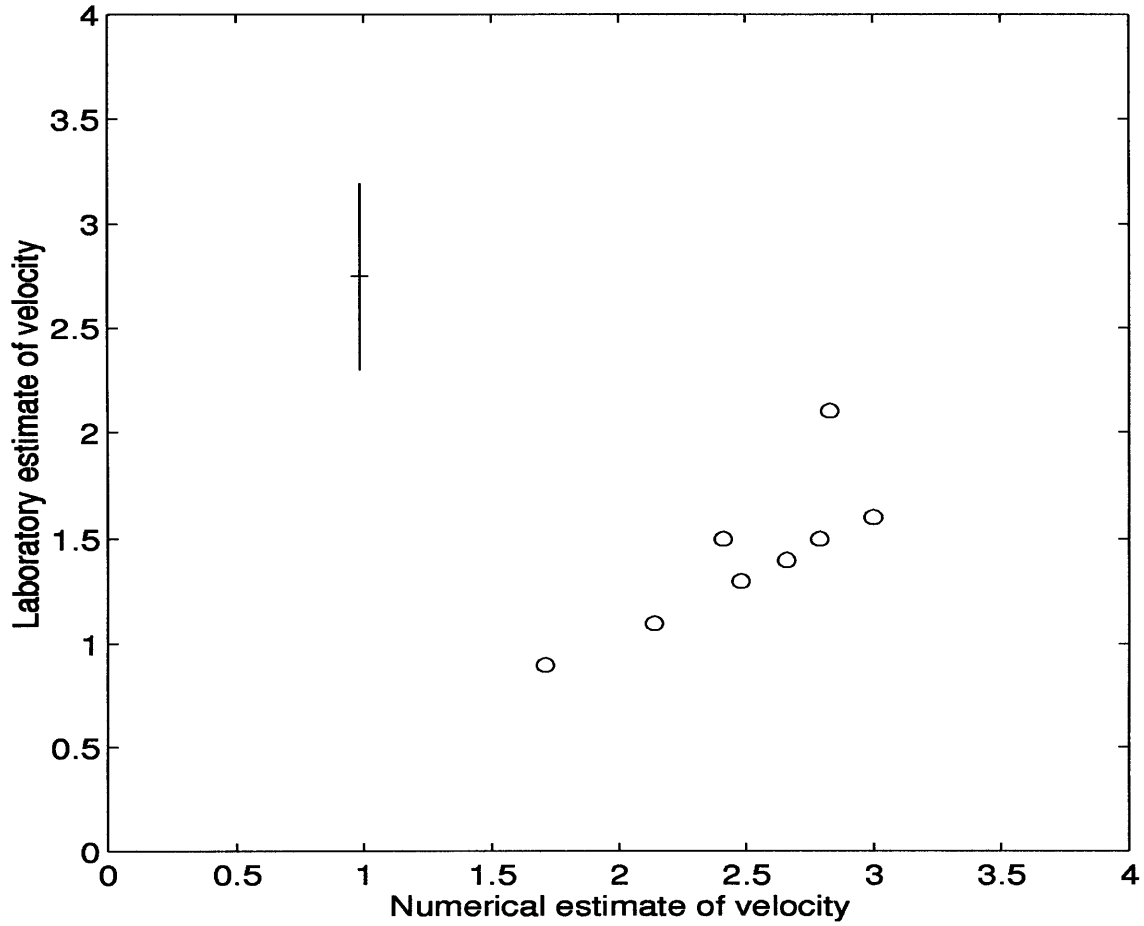Figure 4.3: Comparison between laboratory and numerical estimates of mode number, M^{lab} and M^{num}.

Figure 4.4: Comparison between laboratory and numerical estimates of maximum velocity, u_{rim}^{lab} and u_{rim}^{num}.

Figure 4.4 shows the observations of maximum velocity, from the laboratory u_{rim}^{lab} versus numerics u_{rim}^{num}. The estimates from the numerical experiments are consistently higher than the estimates from the laboratory. This eventuality was discussed above as a possible consequence of the laboratory measurement errors. The fact that the data are so closely grouped and the consistency of the small discrepancy seem to indicate a satisfactory agreement between the laboratory and numerical estimates of horizontal speed.

Figure 4.5 shows the laboratory and numerical observations of eddy length scale l_{eddy}^{lab} and l_{eddy}^{num}. Again as expected, the numerical estimate is consistently larger

than the laboratory estimate. This discrepancy is much larger than that in the velocity data. The discrepancy is $10 - 15cm$. In light of the good linear relationship between the laboratory and numerical estimates it seems more likely to be another symptom of systematic measurement error rather than a symptom of numerical failure. As discussed in section 3.2, the laboratory eddies can only be measured to the extent that a visible dye signature exists. This dye edge may lie closer to the center of the eddy than the edge of the azimuthal velocity field measured in the numerical experiment. Any lag in the time of measurement of the eddies between the laboratory and numerics would only aggravate the issue. The close grouping of the data about a linear relation indicates a satisfactory agreement between the laboratory and numerical data.

Finally, Figure 4.6 shows the comparison between the laboratory and numerical estimates of d_{max}^{lab} and d_{max}^{num}. This figure 4.6 shows that the agreement between the two estimates is approximately one to one, within measurement error. There is some discrepancy at large depths. This may come from the systematic correlation between the numerical estimates of d_{max}^{num} and d_{final}^{num}. We have already established that the laboratory estimate of d_{max}^{lab} does not scale with d_{final}^{scal}, but the numerical estimate of d_{max}^{num} does better, as we will see in the following section. So, the discrepancy is not surprising, it indicates that the numerical estimate of d_{max}^{num} is not a perfect proxy for the laboratory estimate d_{max}^{lab}. However, the discrepancy is small enough for us to draw some useful information from the comparison. The adequate agreement is significant in that it supports the supposition that the individual plumes need not be perfectly resolved in order to accurately simulate chimney evolution. The laboratory presents us with a physical system that must evolve within any existing influence of the plumes. The numerical experiments were not adequately resolving the smallest of the individual plumes. Yet, the vertical evolution of the chimney is in each case virtually identical within measurement error.
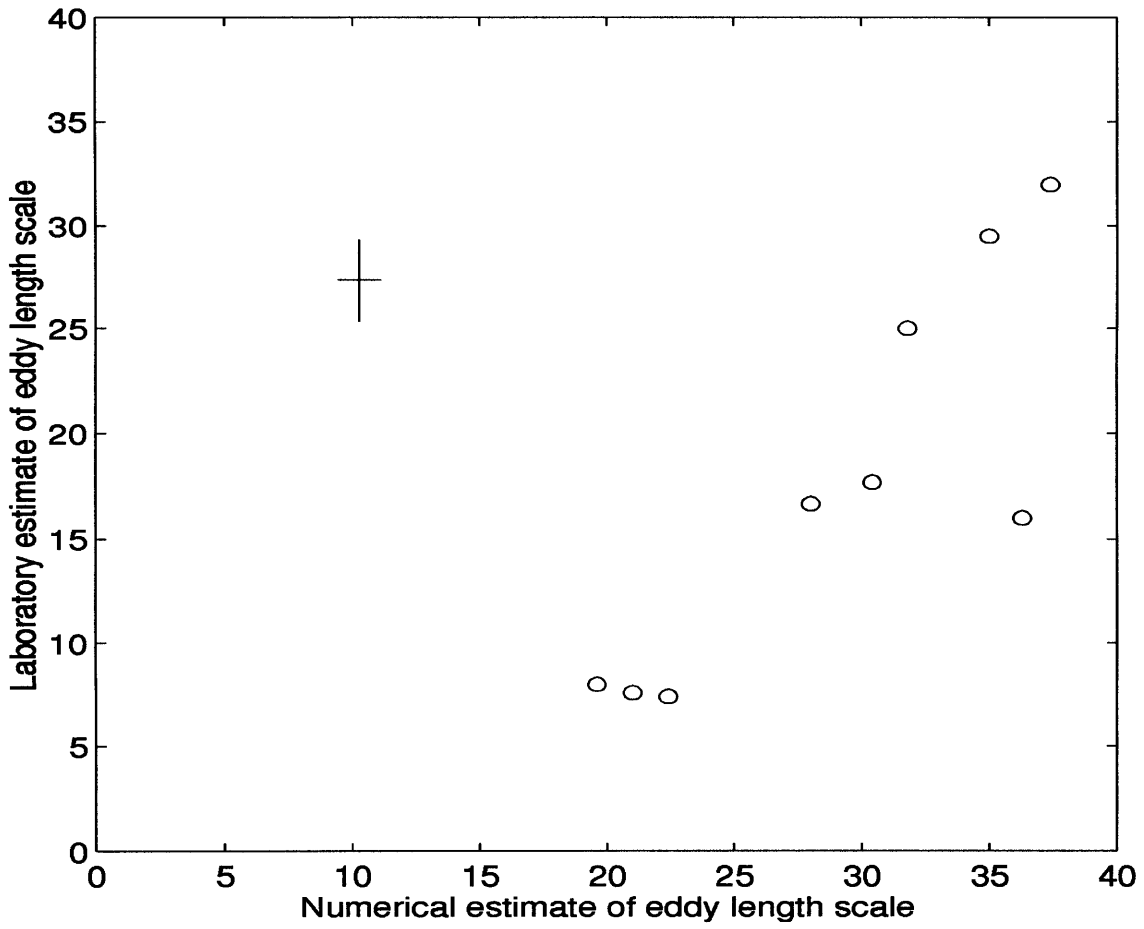
Figure 4.5: Comparison between laboratory and numerical estimates of eddy length scale, l_{eddy}^{lab} and l_{eddy}^{num}.
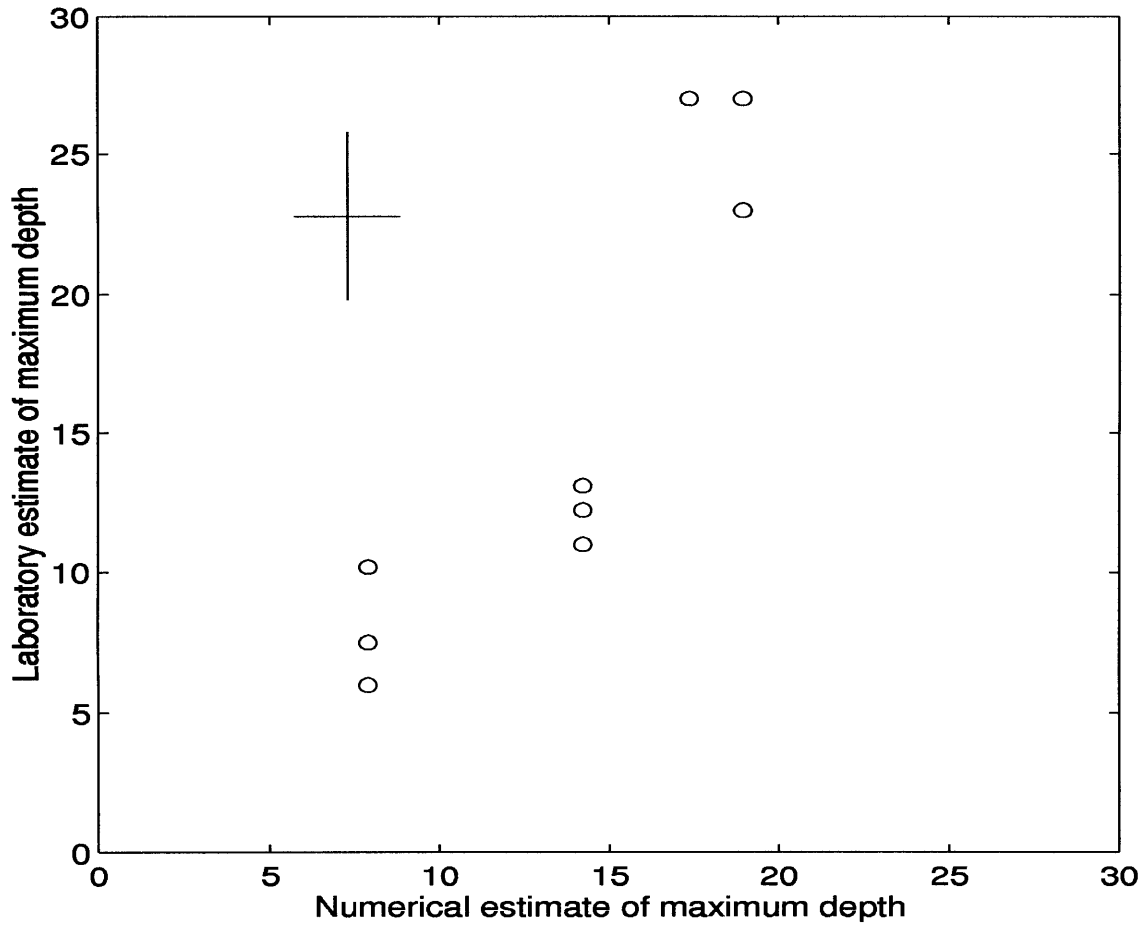
Figure 4.6: Comparison between laboratory and numerical estimates, d_{max}^{lab} and d_{max}^{num}.

4.4 Results

In addition to the measurements made for comparison, numerical estimates were made of d_{final}^{num} over a range of R_s values and a wider range of N and f. At the same time, estimates were made of d_{max}^{num} and V_{final}^{num}, the final volume of dense water produced by the convective event. These quantities are presented in Table 4.3, along with the experimental parameters which were varied; the table also repeats the values of d_{max}^{num} used above for comparison with the laboratory. For all these experiments $B_o = .3cm^2/s^3$, $\nu = 10^{-6}m^2/s$ and $\kappa = 10^{-6}m^2/s$.

Again, as in section 3.3, the observations are scaled by prediction and presented against the non-dimensional numbers. Now we have a range of R_s/H to explore also. The error analysis is identical to that in Chapter 3, with the exception of the V_{final} analysis which will be discussed in detail below. The values of slope, (α) and intercept, (β) are shown in Table 4.4, along with their respective variances (σ_α^2 and σ_β^2). Also tabulated are the 95% confidence limits for the slope.

Figures 4.7, 4.8, and 4.9 show the scaled quantity $\frac{d_{final}^{num}}{d_{final}^{scal}}$ against N/f, R_o^*, and R_s/H respectively. The scaling used here is

$$d_{final}^{scal} = \frac{(B_o R_s)^{1/3}}{N}.$$

In all three cases the zero slope lies within the confidence limits.

The resulting constants of proportionality between the observed and predicted values are 2.2, 2.3 and 2.1. The arguments which led to the relation for d_{final}^{scal} were not capable of determining this constant. The reader should recall that our derivation of this quantity came from an assumption that all of the potential energy in the baroclinic zone would be converted to kinetic energy. Our empirical constant is an indicator of the efficiency of that conversion.

Figures 4.10, 4.11 and 4.12 show the quantity $\frac{d_{max}^{num}}{d_{final}^{scal}}$ versus N/f, R_o^*, and R_s/H. The zero slope lies within the confidence limits only for the cases of R_o^* and R_s/H. In the case of N/f there exists a significantly non-zero positive relationship. In light

Comp run	f	N	R_s (cm)	$d_{max}(cm)$	$d_{final}(cm)$	$Vol_{final}(\%)$
1	0.5000	0.9370	7.5	7.89	4.74	1.08
2	0.5000	0.4310	7.5	11.05	7.89	1.62
3	0.5000	0.2400	7.5	15.79	11.05	2.46
4	0.2500	0.9370	7.5	6.32	3.16	1.43
5	0.2500	0.4310	7.5	11.05	7.89	1.86
6	0.2500	0.2400	7.5	14.21	11.05	2.67
7	0.1250	0.9370	7.5	9.47	3.16	0.87
8	0.1250	0.4310	7.5	11.05	9.47	1.33
9	0.1250	0.2400	7.5	14.21	11.05	2.62
10	0.5000	0.9370	15.0	7.89	6.32	2.34
11	0.5000	0.4310	15.0	14.21	11.05	5.15
12	0.5000	0.2400	15.0	18.95	17.37	6.25
13	0.2500	0.9370	15.0	7.89	6.32	2.86
14	0.2500	0.4310	15.0	14.21	11.05	4.67
15	0.2500	0.2400	15.0	18.95	17.37	7.75
16	0.1250	0.9370	15.0	7.89	4.74	4.52
17	0.1250	0.4310	15.0	14.21	11.05	4.84
18	0.1250	0.2400	15.0	17.37	14.21	8.95
19	0.2500	0.1800	15.0	20.53	17.37	9.72
20	1.0000	0.2400	15.0	20.53	15.79	7.68
21	0.2500	0.4310	22.5	14.21	11.05	7.62
22	0.5000	0.4310	22.5	15.79	11.05	11.18
23	0.1250	0.4310	22.5	14.21	9.47	4.45

Table 4.3: This table displays the raw data for the numerical experiments along with the experimental parameters used for each run.

comparison	α	β	σ_α	σ_β	$\alpha + \epsilon$	$\alpha - \epsilon$
$\frac{d^{num}_{final}}{d^{scal}_{final}}$ vs N/f	0.0882	2.2025	0.0040	0.0116	0.2127	-0.0362
$\frac{d^{num}_{final}}{d^{scal}_{final}}$ vs R^*_o	-0.3614	2.3807	0.2395	0.0123	0.5978	-1.3206
$\frac{d^{num}_{final}}{d^{scal}_{final}}$ vs R_s/H	0.3825	2.1379	0.2296	0.0551	1.3216	-0.5566
$\frac{d^{num}_{max}}{d^{scal}_{final}}$ vs N/f	0.2882	2.5550	0.0040	0.0116	0.4127	0.1638
$\frac{d^{num}_{max}}{d^{scal}_{final}}$ vs R^*_o	-0.1222	2.9502	0.2395	0.0123	0.8369	-1.0814
$\frac{d^{num}_{max}}{d^{scal}_{final}}$ vs R_s/H	0.2266	2.8226	0.2296	0.0551	1.1658	-0.7125

Table 4.4: Measured parameters of least squares fit to the data. Observational data was divided by scaling prediction, the resulting value was compared to the non-dimensional numbers N/f and R^*_o. Shown here are the estimates of the slope, α, the intercept, β, and their associated variance, σ_α and σ_β, and the confidence intervals on the slope estimate $\alpha^+_-\epsilon$ where $\epsilon = 1.97 \times \sigma_\alpha^{1/2}$.
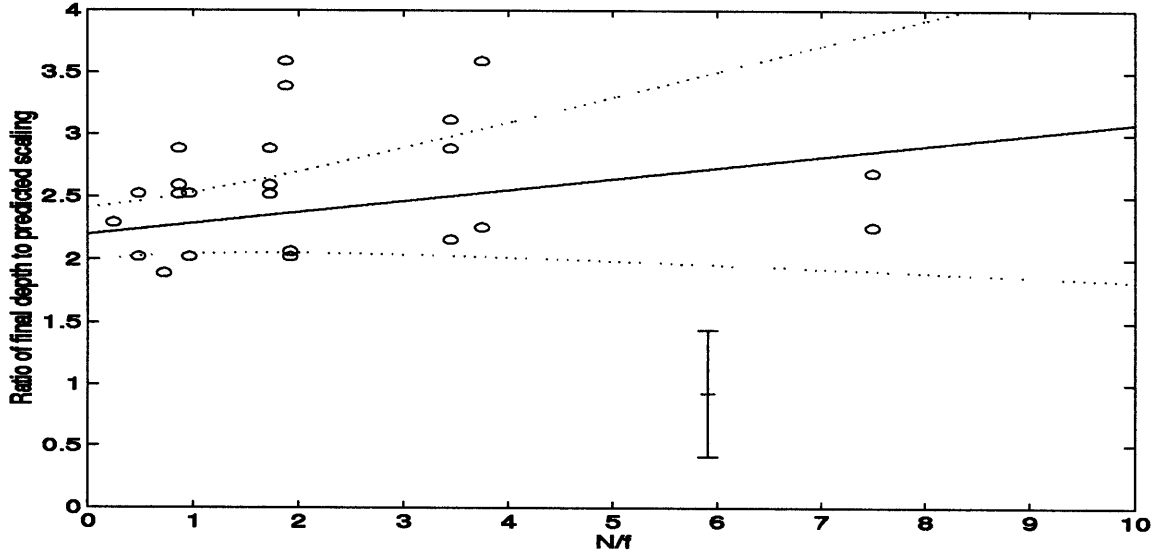

Figure 4.7: Numerical value of $\frac{d^{num}_{final}}{d^{scal}_{final}}$ plotted against N/f.
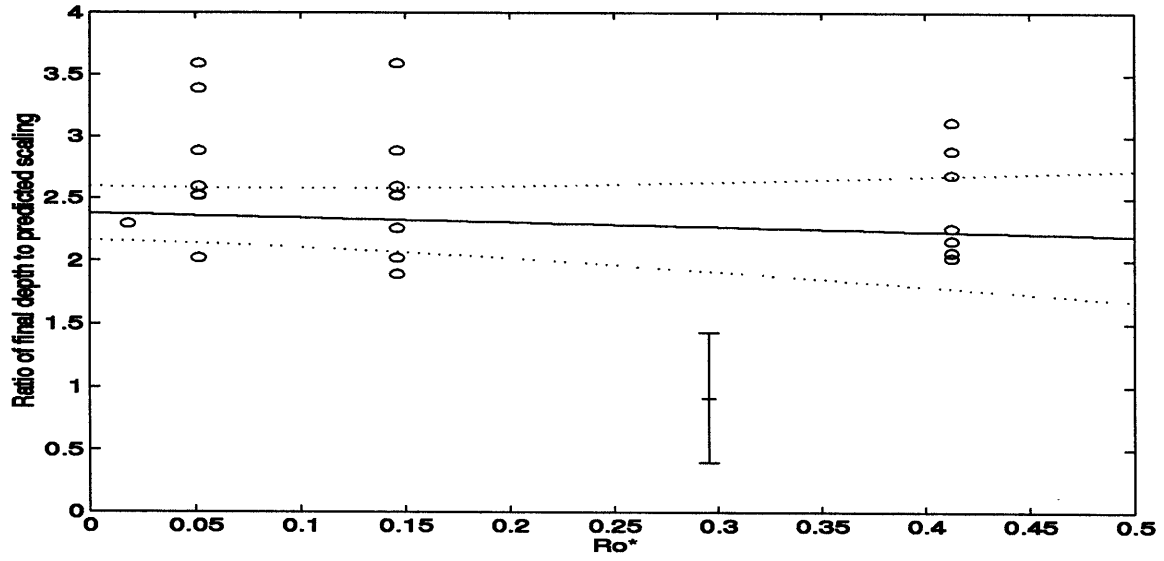
Figure 4.8: Numerical value of $\frac{d_{final}^{num}}{d_{final}^{scal}}$ plotted against R_o^*.
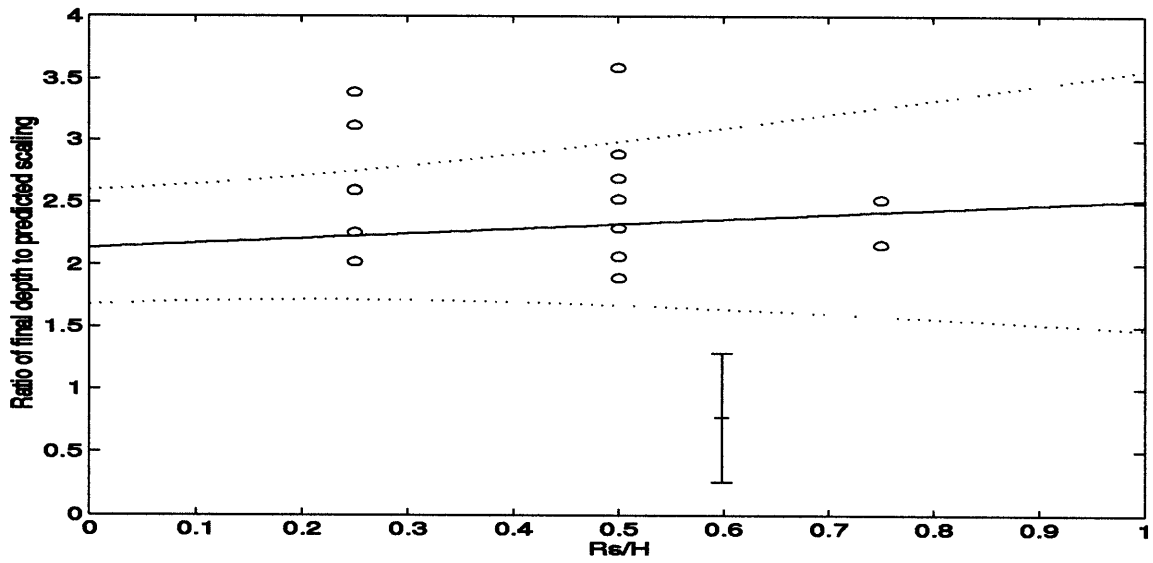

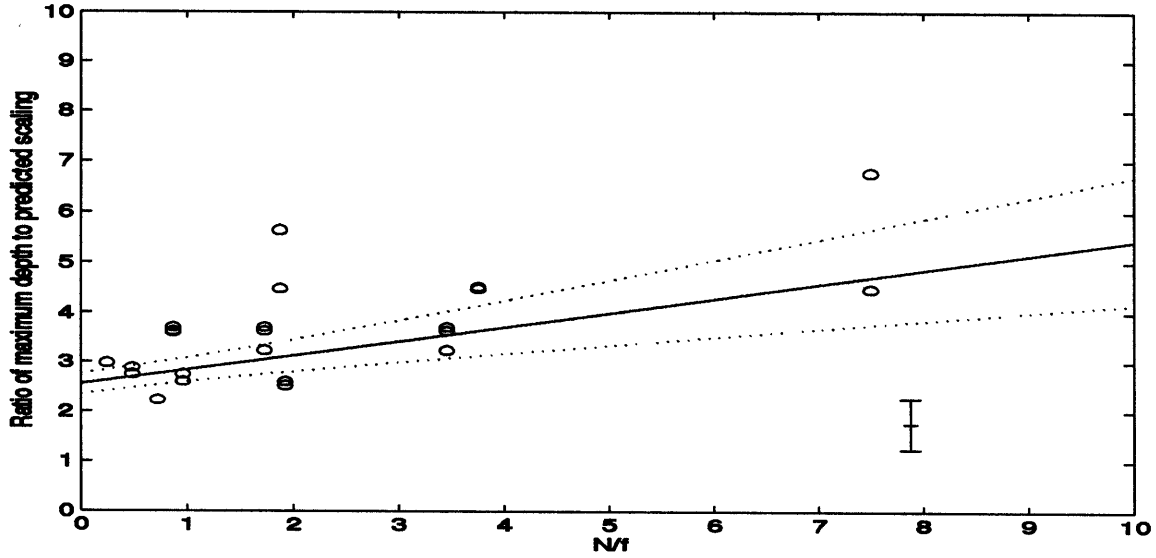Figure 4.9: Numerical value of $\frac{d_{final}^{num}}{d_{final}^{scal}}$ plotted against R_s/H.

Figure 4.10: Numerical value of $\frac{d_{max}^{num}}{d_{final}^{scal}}$ plotted against N/f.

of the successful agreement of our estimate of d_{final}^{num} with scaling, the discrepancy between d_{max}^{num} and d_{final}^{scal} seems to indicate an inadequacy in our definition of d_{max}^{num}, or our choice of d_{max}^{num} as a proxy for d_{final}^{num}, as opposed to an inadequacy in the scaling. From Table 4.3 we see that the constants of proportionality relating d_{max}^{num} to d_{final}^{scal} are slightly larger than those relating d_{final}^{num} with d_{final}^{scal}, again owing to definition.

Figures 4.13, 4.14 and 4.15 show the measured quantity V_{final}^{num} divided by the predicted value of $V_{final}^{scal} = \pi R_s^{4/3} d_{final} B_o^{1/3} \times t$, versus N/f, R_o^*, and R_s/H. As stated above, the values of V_{final}^{num} were measured only at one time; therefore the appropriate scaling depends on a constant value of time, incorporated here in the constant of proportionality. This fit tests only the dependence of V_{final}^{num} on the predicted rate of production. There is no significant measurement uncertainty associated with estimate of volume. A non-weighted linear regression on this data indicates that there is no significant non-zero trend in any of the three cases, with 95 % confidence. In the comparison with N/f the estimated slope is $\alpha = 1.7846$ and the estimated intercept is $\beta = 19.0706$.
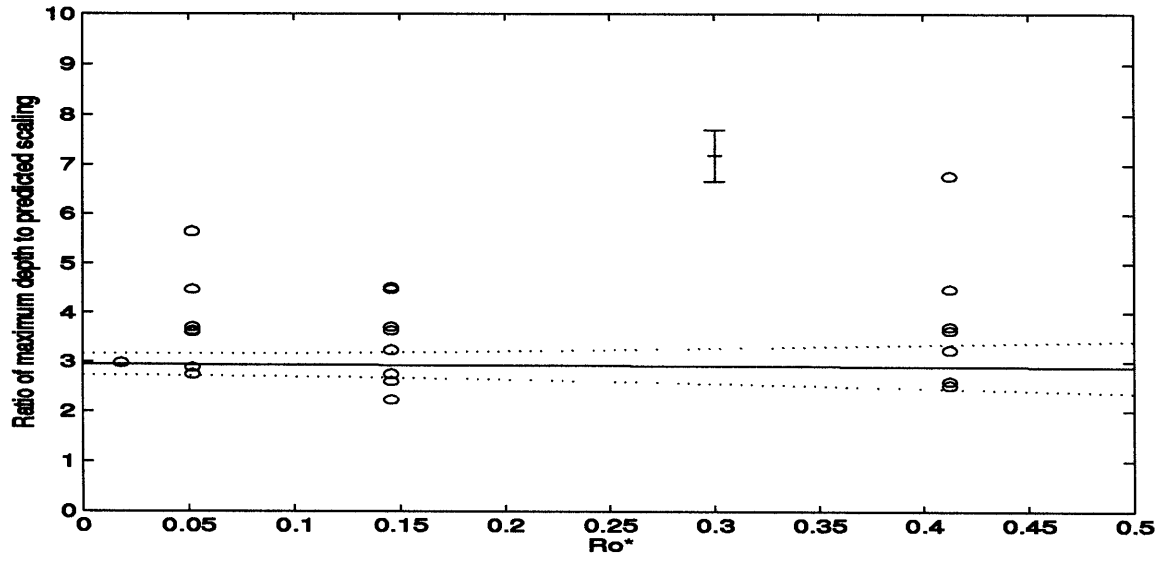
61

Figure 4.11: Numerical value of $\frac{d_{map}^{num}}{d_{final}^{scal}}$ plotted against R_o^*.
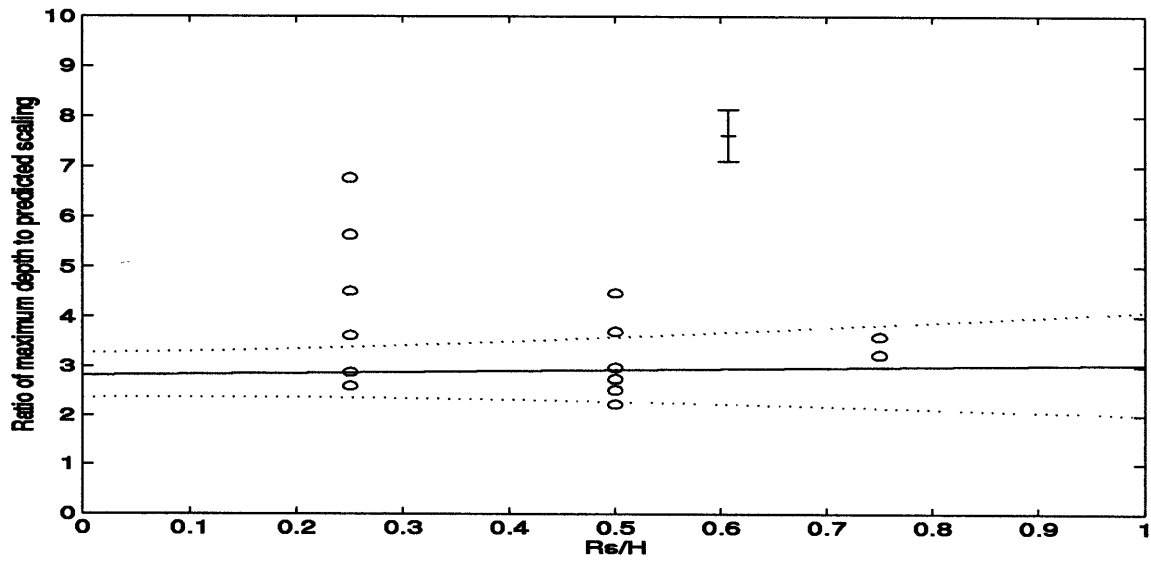

Figure 4.12: Numerical value of $\frac{d_{map}^{num}}{d_{final}^{scal}}$ plotted against R_s/H.

Figure 4.13: Numerical value of $\frac{V_{final}^{num}}{V_{final}^{scal}}$ plotted against N/f.

In the comparison with R_o^* the estimated slope is $\alpha = 6.3557$ and the estimated intercept is $\beta = 21.8819$.

In the comparison with R_s/H the estimated slope is $\alpha = -18.2357$ and the estimated intercept is $\beta = 31.0357$. Again, in each of the three cases, the slope is not statistically different from zero within 95 % confidence.

Figure 4.14: Numerical value of $\frac{V_{final}^{num}}{V_{final}^{scal}}$ plotted against R_o^*.

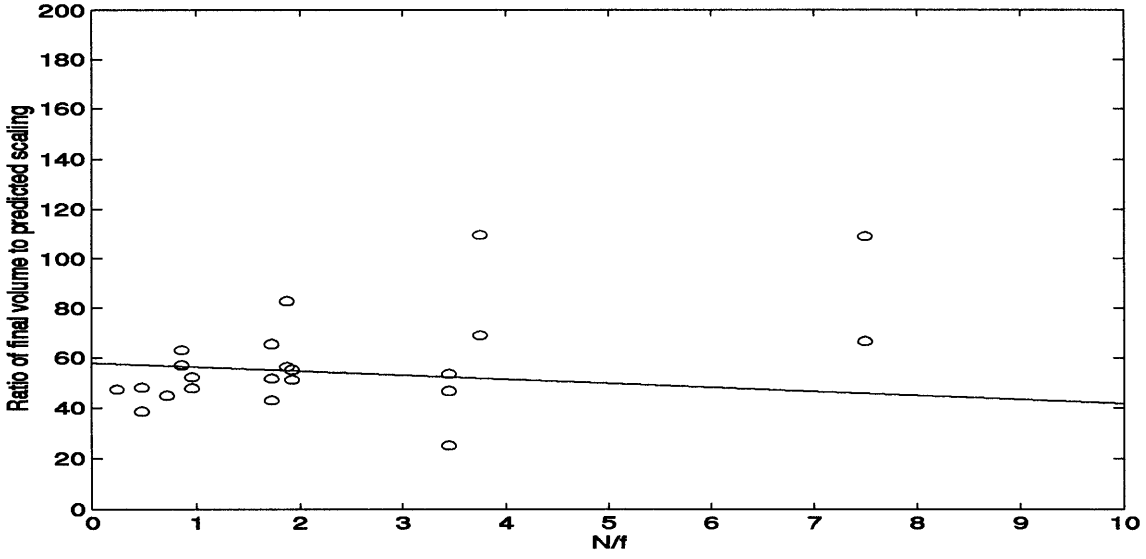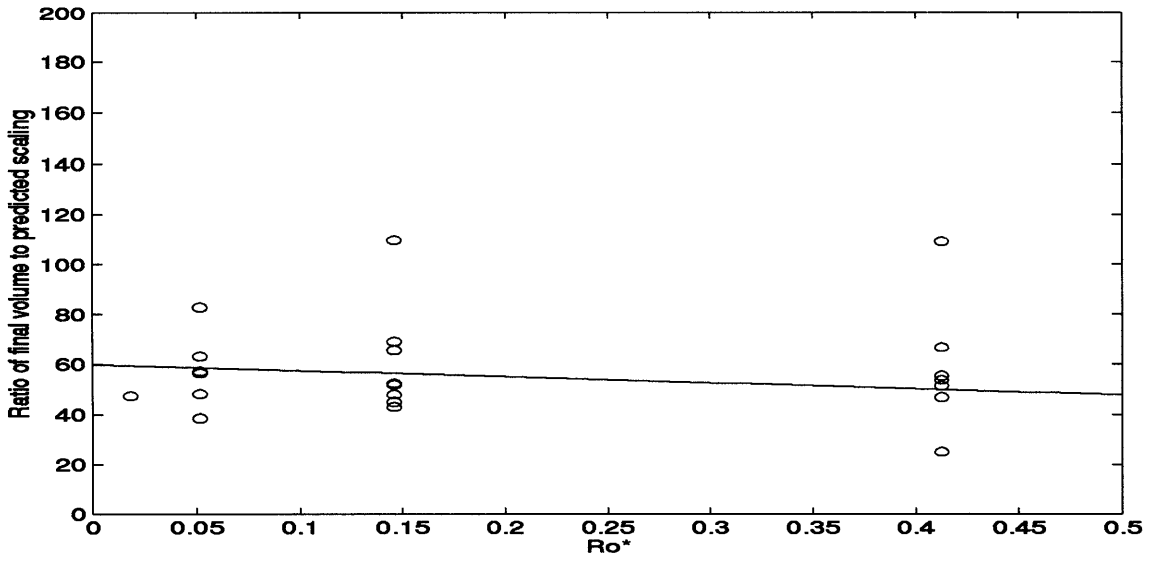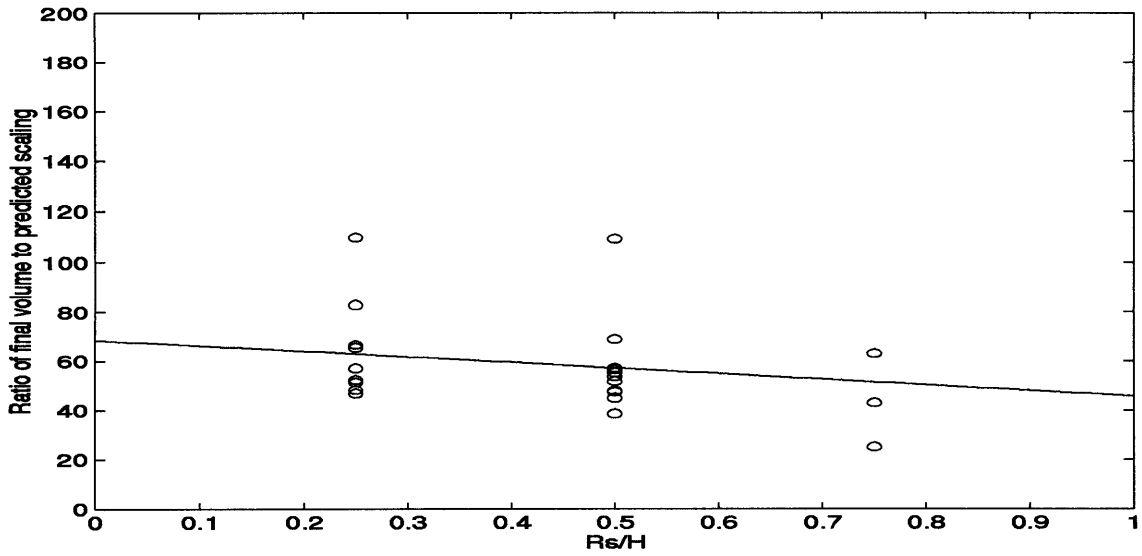Figure 4.15: Numerical value of $\frac{V_{final}^{num}}{V_{final}^{scal}}$ plotted against R_s/H.

64

Chapter 5

Discussion

The quantities estimated from the numerical model compared satisfactorily with the laboratory observations. There were some discrepancies, but none which contradicted the premise that the numerical model is adequately resolving the relevant physics we have chosen to consider in our problem.

The laboratory and numerical experiments agree best in estimates of mode number. The laboratory observations of this quantity agree very well with the predicted scaling. This was expected, given that mode number is well understood. However it is encouraging in its validation of the numerical model.

The estimates of maximum velocity from the laboratory and numerics agree well with each other, although the laboratory measurement is a consistent underestimate of the numerical value. The laboratory observations are associated with very large measurement uncertainty. Within the limits of that uncertainty they agree excellently with the predicted scaling.

The numerical and laboratory estimates of l_{eddy} also agree well, while the laboratory definition is again an underestimate of the numerical value. The laboratory estimates of l_{eddy}^{num} agree well with the predicted scaling only if one chooses $h \sim d_{final}^{scal}$ as the appropriate scale for depth. That is, one must use the calculated prediction of d_{final}^{scal} since there is no laboratory observation of this quantity. The measurement of

65

d_{max}^{lab} is not an adequate proxy. If one uses $h \sim d_{max}^{lab}$ then l_{eddy}^{lab} does not agree with the predicted scaling.

The laboratory and numerical estimates of d_{max} did not compare as well as the estimates of other quantities. This seems to be an artifact of the definitions of d_{max}^{num} and d_{final}^{num}. The laboratory estimates of d_{max}^{lab} did not agree with the predicted scaling for d_{final}^{scal}. The laboratory measure of d_{max}^{lab} reflects all overshooting and oscillation past the spreading level. This is not the quantity we actually wanted to measure. We are interested in the level of the bulk of the dense water. To observe this more accurately, the laboratory apparatus could have been left running for several hours after the forcing was terminated. The convectively produced water would gradually rebound to its neutrally buoyancy level. A measurement at that time would more closely estimate our quantity d_{final}^{scal}.

The numerical estimates of d_{final}^{num} agree well with the predicted scaling for that quantity. This agreement supports our choice of $L = \frac{Nh}{f}$ as the length scale for Δy the distance across the baroclinic zone. It also validates our assumption of thermal wind balance in the convective region. It is interesting to note that while we are describing the impact of baroclinic instability on mixed layer depth, the relation does not depend explicitly on f. According to our results, the final depth of the convectively produced water depends only on the size and intensity of the forcing and the ambient stratification. Implicit in the derivation of this quantity d_{final}^{scal} is the balance between buoyancy forcing at the surface and the lateral transport of dense fluid by baroclinic eddies. Again recall that one of the most important ramifications of the calculated constant of proportionality for d_{final}^{num} is an indication of the efficiency of the baroclinic transport. The quantity was derived from the energy balance assuming that all available potential energy was converted to kinetic energy. The constant of proportionality between d_{final}^{num} and d_{final}^{scal} is a gauge of the accuracy of that assumption. This balance then is important not only in the matter of convection, but also

anywhere that the efficiency of baroclinic eddies is of interest, for example in the parameterization of baroclinic eddies for use in coarse–scale models.

In the case of convection, where forcing persists long enough for the formation of baroclinic eddies, the scales summarized here will govern the evolution of a convective chimney:

$$M^{scal} = \frac{\sqrt{8}R_s f}{N d_{final}},$$

$$v_{max}^{scal} = \sqrt{2B_o/f},$$

$$l_{eddy}^{scal} = \frac{N d_{final}}{f},$$

and

$$d_{final}^{scal} = \frac{(B_o R_s)^{1/3}}{N}.$$

The data from both laboratory and numerical experiments support these scalings. To see when these scalings would be relevant we need to take a closer look at the magnitude of "long enough". Recall that the shortest time necessary for the chimney to evolve to d_{final} is given by

$$t = \frac{2.3}{\sqrt{2}} \left(\frac{R_s^2}{B_o} \right)^{1/3},$$

using our empirical constant of proportionality for d_{final} and the $\sqrt{2}$ from the one dimensional derivation. Using our above values for a typical Meditteranean event $B_o \approx 800W/m^2$ over an area $R_s = 20 - 45km$ we find $t = 2 \times 10^5 s$, or $\approx 5 days$. The Mistral typically persist for up to a week however, forcing this strong rarely persists for more than 1–2 days. Therefore, it is unlikely that baroclinic eddies are impacting the evolution of Meditteranean deep water.

Now let us look at some typical values for the Labrador Basin. We will consider the conditions at weather station Bravo as typical of the entire basin. There is some evidence that the buoyancy flux measured here is typical of the basin based on analyzed fields from European Center for Medium–Range Weather Forecasting (ECMWF), [Pickart, 1994]. Then choosing average winter values from the Bravo

records for several years we find for warm winters a basin wide heat loss of $100W/m^2$, and for extreme cold winters values of $600W/m^2$. These heat losses persist for a month or more.

Using a value of buoyancy frequency calculated from CTD data [Pickart, 1994] it is reasonable to assert that the ambient stratification encountered by the convective overturning is $N \approx 9 \times 10^{-4}s^{-1}$. Using these values and the dimensions of the basin ($R_s \approx 500km$) we find the case of $B_o = 100W/m^2$, to corresponds with a depth $d_{final} = 690m$ with a minimum formation time of $t_{final} = 33.5days$. The case of $B_o = 600W/m^2$ corresponds with a final depth $d_{final} = 1260m$ and a minimum formation time of $t_{final} = 18.5days$. Note that the stronger the forcing the faster the convective penetration and the deeper the mixing.

The depths predicted above are roughly consistent with recorded depths of mixing at Bravo [Lazier, 1980]. For example, the estimate of $100W/m^2$ is appropriate to winter 1968, where the recorded depth of mixing was $800m$ and we predicted $690m$. Winter 1972 was extremely cold, $B_o \approx 800W/m^2$. That winters recorded depth of mixing was $1500m$ where we predicted $1260m$.

Given these estimates it seems likely that Labrador Sea overturning is affected by the processes studied here. In that case, baroclinic eddies formed at the edges of the convection site, ie. the edge of the basin, provide an appealing mechanism for the transfer of convectively produced water into the DWBC.

One might also expect that the final volume of convectively produced water manufactured by one of these events would also be governed by the above scaling theories. The numerical estimates of V_{final} agreed well with the proposed dependence on rate

$$rate_{max} = R_s^{4/3}B_o^{1/3}d_{final} = \frac{R_s^{5/3}B_o^{2/3}}{N},$$

recall that the final volume is assumed to depend on the maximum rate of production and the duration of the forcing

$$V_{final} = rate_{max} * t,$$

68

where our measurements were taken at $t = 300\ s$. This scaling indicates that the final volume of water produced will depend on the size of the forcing area and the final depth of penetration, or more explicitly it will depend on the size and intensity of the forcing, and the initial stratification.

The final volume of water produced is of interest in observations of the Labrador Sea. There exist volume estimates of water produced by convection in the Labrador Sea. This Labrador Sea Water (LSW) is associated with the Deep Western Boundary Current (DWBC) as it leaves the Labrador Basin, and transports have been calculated from hydrographic sections through the current. However, very little is known about the frequency, duration or position of convective events in the Labrador Sea. It is not clear that water with the characteristics of LSW is produced every year; but the signal of LSW associated with the DWBC is relatively steady. In unraveling these questions it will be useful to understand how much water to expect from a given convection event; and to know that the estimate may be made given a hydrographic survey of the ambient stratification of the region, and meteorological surveys of typical storms.

Bibliography

[Brugge et al., 1991]

Brugge, R., H.L. Jones and J.C. Marshall, 1991: Non-hydrostatic ocean modeling for studies of open-ocean deep convection. *Deep Convection and Deep Water Formation in the Oceans*, Chu & Gascard (editors), Elsevier Science Publishers.

[Bubnov and Senatorsky, 1988]

Bubnov, B.M. and A.O. Senatorsky, 1988: Influence of boundary conditions on convective stability of horizontal rotating fluid layer. *Izu. Akad. Nauk. SSSR Mech. Zhid. i Gaza*, **3**, 124–129.

[Chandrasekhar, 1953]

Chandrasekhar, S., 1953: The instability of a layer of fluid heated below and subject to Coriolis forces. *Proc. R. Soc. Lond. A*, **217**, 306–327.

[Eady, 1949]

Eady, E.T., 1949: Long waves and cyclone waves. *Tellus*, **1**, 33–52.

[Gill, 1982]

Gill, A., 1982: *Atmosphere-Ocean Dynamics*, Academic Press, San Diego, pp. 662.

[Green, 1970]

Green, J. S. A., 1970: Transfer properties of the large–scale eddies and the general circulation of the atmosphere. *Quart. J. Roy. Meteor. Soc.*, **96**, 157–185.

[Helfrich and Send, 1988]

Helfrich, K., and U. Send, 1988: Finite-amplitude evolution of two-layer geostrophic vortices. *J. Fluid Mech.*, **197**, 331–348.

[Ivey et al., 1993]

Ivey, G. N., J. R. Taylor, and M. J. Coates, 1993: Convectively driven mixed layer growth in a rotating, stratified fluid. *Deep–Sea Res.*, submitted.

[Jones and Marshall, 1993]

Jones, H., and J. Marshall, 1993: Convection with rotation in a neutral ocean: A study of open-ocean deep convection. *J. Phys. Oceanogr.*, **23**, 1009–1039.

[Klinger, 1994]

Klinger, B. A., 1994: Representation and parameterization of deep convective plumes by mixing. *J. Phys. Oceanogr.*, submitted.

[Lazier, 1980]

Lazier, J. R. N., 1980: Oceanographic conditions at ocean weather ship Bravo, 1964–1974. *Atmosphere–Ocean*, **18**, 227–238.

[Leaman and Schott]

Leaman, K.D., and F. Schott, 1991: Hydrographic structure of the convection regime in the Gulf of Lions: Winter 1987. *J. Phys. Oceanogr.*, **21**, 573–596.

71

[Legg and Marshall, 1994]   Legg, S., and J. Marshall, 1993: A heton model of the spreading phase of open-ocean deep convection. *J. Phys. Oceanogr.*, **23**, 1040–1056.

[Marshall, Whitehead and Yates, 1994]   Marshall, Whitehead and Yates, 1994: Laboratory and numerical experiments in oceanic convection. *Ocean Processes in climate Dynamics: Global and Mediterranean Examples*, Malanotte-Rizzoli and Robinson (editors), Kleuver Academic Publishers, pp. 437.

[Maxworthy and Narimousa, 1994]   Maxworthy, T. and S. Narimousa, 1992: Unsteady, turbulent convection into a homogeneous, rotating fluid, with oceanographic application. *J. Phys. Oceanogr.*, submitted.

[MEDOC, 1970]   MEDOC, 1970: Observation of formation of deep water in the Mediterranean Sea. Nature **227**, 1037–1040.

[Nakagawa and Frenzen, 1955]   Nakagawa, Y. and P. Frenzen, 1955: A theoretical and experimental study of cellular convection in rotating fluids. *Tellus*, **7**, 1–21.

[Pedlosky, 1985]   Pedlosky, J., 1985: The instability of continuous heton clouds. *J. Atmos. Sci.*, **42**, 1477–1486.

[Pickart, 1994]   Pickart, R., 1994, personal correspondence.

[Saunders, 1973]   Saunders, P. M., 1973: The Instability of a Baroclinic Vortex. *J. Phys. Oceanogr.*, **3**, 61–65.

[Schott, et al., 1992]   Schott, F., M. Visbeck, and J. Fischer, 1992: Observations of vertical currents and convection in the central Greenland Sea during the winter of 1988/89. *J. Geo. Phys. Res.*, **98**, 14,401–14,421.

[Talley and McCartney, 1982]   Talley, L. D. and M. S. McCartney, 1982: Distribution and circulation of Labrador Sea Water. *J. Phys. Ocea.*, **12**, 1189–1205.

[THETIS, 1994]   THETIS, 1994: Open-Ocean Deep Convection Explored in the Mediterranean. *EOS*, **75**, No. 19, 217–221.

[Visbeck and Marshall, 1994]   Visbeck, M. and J. Marshall, 1994, Steady state open ocean convection: Scales and eddy flux parameterization, (**draft**)

Appendix I

There is one other point of interest regarding the occurrence of heton pairs in our experiments. The term heton pair refers to the phenomenon of lateral separation of the surface cyclone and the subsurface anti-cyclone. In some regimes we see a baroclinic eddy whose sole surface signature is cyclonic, with an anti-cyclonic circulation present only at depth. Such cases can be seen in several of our numerical and laboratory experiments and in oceanic regimes described in [Jones and Marshall, 1993].

However, in regimes of high mode instability we see the lateral separation of the two circulations, and a surface signature associated with the anti-cyclone. The cyclonic circulation is always the strongest at the surface, and is often the stronger of the pair, extending to depth. The anti-cyclone is always strongest at depth and is occasionally too weak to be visible at the surface. Figure 5.1 displays a map of the numerical experiments in which the lateral separation of the eddies was manifest.
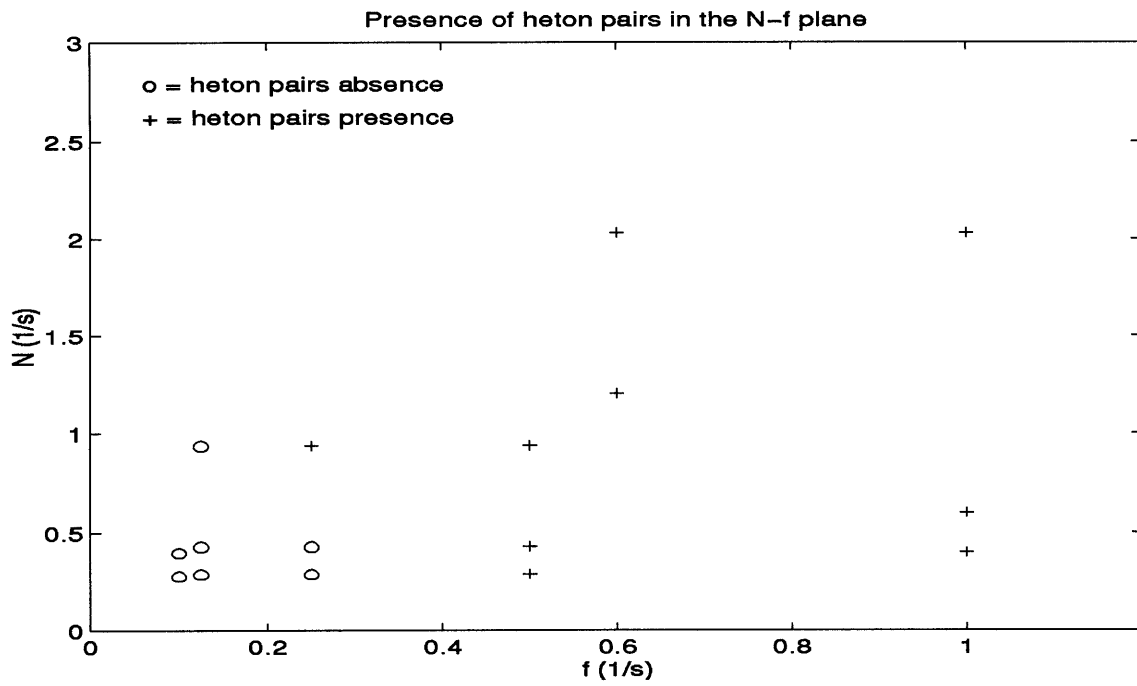
Figure 5.1: Map showing the experiments performed on the computer as seen in N-f space; experiments in which hetons were evident are denoted by the + symbol, those in which hetons were not apparent are denoted by the o symbol.